Towards Photonic Integrated Circuits; Design and Fabrication of Passive InP Waveguide Bends

by

Sarah J. Rodriguez

B.E. Engineering Physics
Stevens Institute of Technology 2002

Submitted to the Department of Electrical Engineering and Computer Science in partial fulfillment of the requirements for the degree of
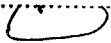
Master of Science in Electrical Engineering

at the
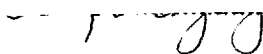MASSACHUSETTS INSTITUTE OF TECHNOLOGY

June 2004

Author ....
Sarah J. Rodriguez
Department of Electrical Engineering and Computer Science
May 20, 2004

Certified by ....
Leslie A. Kolodziejski
uter Science
Supervisor

Accepted by ....
Arthur C. Smith
Chairman, Department Committee for Graduate Students
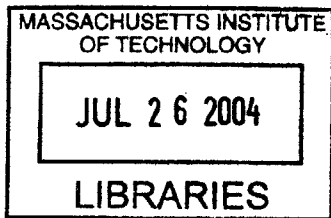
BARKER

Towards Photonic Integrated Circuits; Design and Fabrication of Passive InP Waveguide Bends

by

Sarah J. Rodriguez

ABSTRACT

Waveguide bends, in the (In,Ga)(As,P) material system, have been simulated, fabricated and tested. A process is developed for waveguides of $1\mu m$ through $7\mu m$ widths. Waveguides containing S-bends of varying bending radii as well as resonator bends were examined. Inconsistent measurement results were obtained. Improved measurement methods have been suggested.

Thesis Supervisor: Leslie A. Kolodziejski
Professor of Electrical Engineering and Computer Science

Acknowledgements

Table of Contents

List of Figures

1.0 INTRODUCTION

Efforts for improving communication systems have been made for centuries, starting with written communication systems to modern optical network systems. There is a constant need for making networks with lower loss, higher speed and low cost. Photonic integrated circuits (PIC) provide an efficient way for meeting these demands. PICs will eliminate the need for separate components in the network and perform all of the necessary functions on a single chip, such as amplification, switching, transmitting and receiving to name a few.

Photonic integrated circuits provide a valuable integrated technology platform for use in optical communications. PICs may consist of a number of devices, such as lasers and isolators to name a few, integrated with the use of waveguides.

FIGURE 1.1   Unit optical logic cell
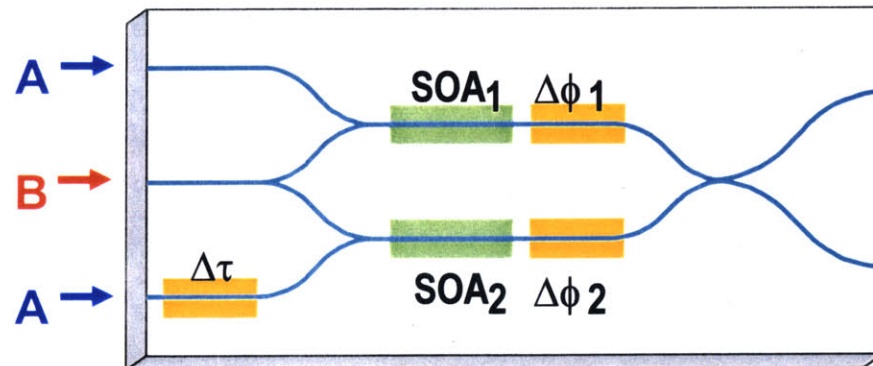
Figure 1.1 depicts an optical logic cell with the blue lines representing the waveguides. One of the major design issues associated with waveguides is the amount of space required for waveguide bends. While tighter bends require less space, they are more prone to radiation loss. In order to reduce the overall size of future PICs, a compact low loss solution to waveguide bending must be found.

This thesis will focus on low loss waveguide bending. Waveguide bends will be simulated, designed, fabricated and tested. Chapter 2 will contain an overview of the theory behind dielectric waveguides, a survey of past research on the topic, simulated results and the design of the waveguide bends. Chapter 3 contains a brief overview of the fabrication process while, Chapter 4 contains the processes in more detail with results. Measurement procedures and the experimental data of

the fabricated waveguides are discussed in Chapter 5. A summary and conclusion of this work is contained in Chapter 6.

2.0 DESIGN THEORY & SIMULATION

2.1 Waveguide Theory

2.1.1 Total Internal Reflection

There are many considerations which must be taken into account while designing waveguides. One concept of importance is total internal reflection. Figure 2.2 depicts the concept of total internal reflection through the use of a ray diagram of an optical fiber.

FIGURE 2.2   Light confinement through total internal reflection in a step-index fiber [1]
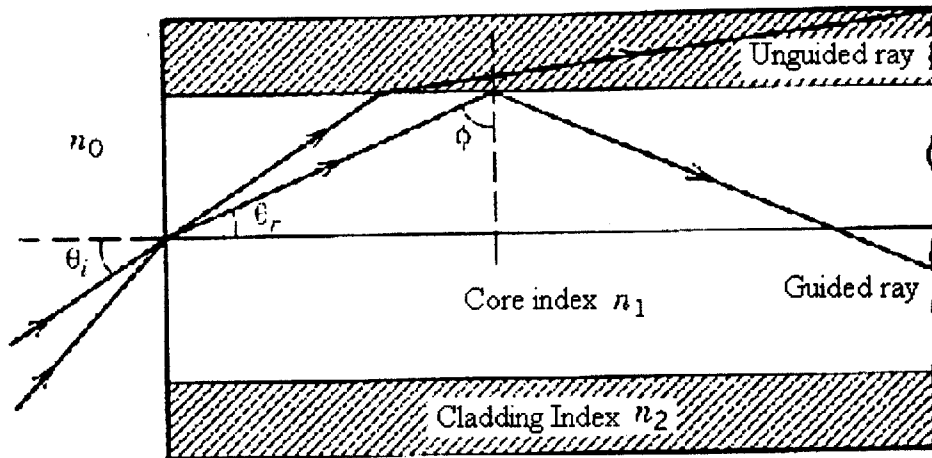
As the diagram shows, the unguided ray is transmitted through the core index into the cladding index. The guided ray is completely reflected throughout the fiber, remaining in the core index. It would be ideal to have information travel in optical waveguides through guided rays, greatly reducing loss.

In order to get a better understanding for how total internal refection takes place, attention is focused on plane waves incident upon a planar boundary. Figure 2.3 illustrates a transverse electric (TE) wave incident at an angle θ upon a boundary. k represents the propagation vector of the traveling wave. The subscripts i, r and t represent the incident, reflected and transmitted components of the wave respectively. For simplicity, the place of incidence is defined in the x-z plane. Upon inspection of the diagram, the propagation vector may be written as follows:

$$\bar{k}_i = \hat{x}k_{ix} + \hat{z}k_{iz}$$

(EQ 2.1)

$$\bar{k}_r = \hat{x}k_{rx} - \hat{z}k_{rz} \qquad \text{(EQ 2.2)}$$

$$\bar{k}_t = \hat{x}k_{tx} + \hat{z}k_{tz} \qquad \text{(EQ 2.3)}$$

FIGURE 2.3 TE wave incident upon a planar boundary [2]

$$H_{rz} = -(E_r/\eta_0) \sin \theta_r$$

$$H_{rx} = -(E_r/\eta_0) \cos \theta_i$$

$$H_{ix} = (-E_0/\eta_0) \cos \theta_i$$

$$H_{iz} = (E_0/\eta_0) \sin \theta_i$$
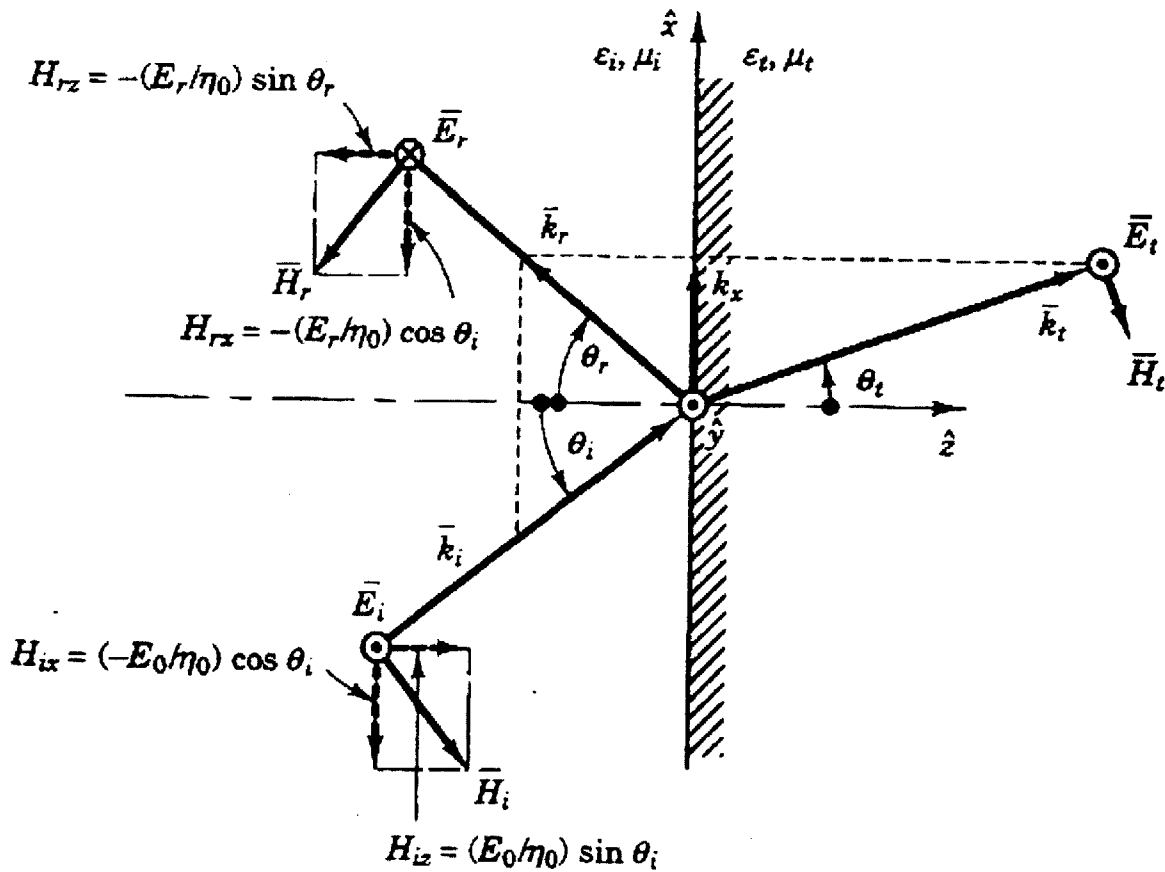
The phase matching condition states the tangential components of the electric and magnetic fields must be continuous for all x and time. Therefore, the tangential components for all three k vectors must be equal along the boundary, leading to equation [2.4].

$$k_x = k_i \sin \theta i = k_r \sin \theta r = k_t \sin \theta t \qquad \text{(EQ 2.4)}$$

Since the reflected and incident wave travel in the same medium, they have the same dispersion relation, therefore the magnitudes of their propagation vectors are equal. From Eq. [2.4], since the magnitudes of the propagation vectors are equal, the incident and reflected angles are also equal, which leads to the following equation:

$$\frac{\sin \theta t}{\sin \theta i} = \frac{n_i}{n_t} \qquad \text{(EQ 2.5)}$$

Equation 2.5 is commonly referred to as Snell's law. Snell's law demonstrates how the relation between the angle of transmission and reflection are dependent on the indices of refraction of both the incident and transmitted medium. Figure 2.4 portrays a pictorial description of Snell's Law.

FIGURE 2.4   (a) Illustrates the case where the transmitting medium has a higher refractive index than the medium in which the incident wave travels. (b) Illustrates the case where the transmitting medium has a lower refractive index than the medium in which the incident wave travels [3]

(a) nl < n2   (b) nl > n2
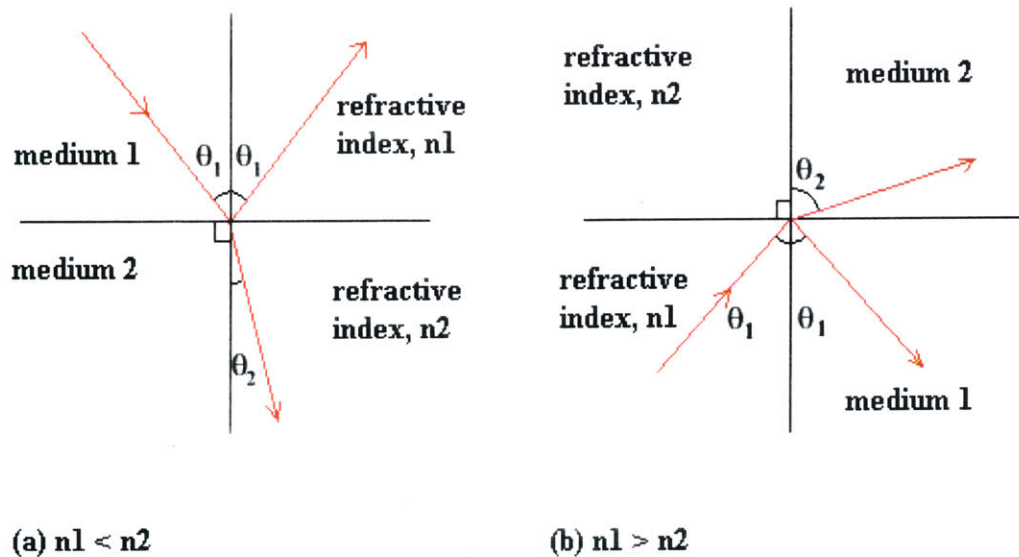
In Figure 2.4 (a), an incident wave travels from a lower index of refraction medium to a higher index of refraction medium. Figure 2.4 (b) portrays the opposite case of an incident wave traveling from a higher index of refraction medium to a lower index of refraction medium. As seen from the diagram, a light ray traveling from an index of higher refraction to an index of lower refraction, will bend further away from the normal of the boundary surface.

In the case of Figure 2.4 (b), if the value of θ_1 were to be increased, there would be a certain value, θ_c where total internal reflection would take place. θ_c is commonly known as the critical angle. When the incident angle equals the critical angle, the transmitted angle equals 90°, therefore the light propagates parallel to the boundary surface. In the case of $\theta_1 = \theta_c$, Snell's law gives us the following result:

$$\frac{\sin\theta_t}{\sin\theta_c} = \frac{1}{\sin\theta_c} = \frac{n_i}{n_t} \qquad \text{(EQ 2.6)}$$

$$\theta_c = arc\sin\left(\frac{n_t}{n_i}\right) \qquad \text{(EQ 2.7)}$$

For θ_1 values larger than θ_c, the transmitted wave exponentially decreases from the boundary surface, this is called an evanescent wave. Since no average power is transmitted into the second medium, in the case of evanescent waves, total internal reflection is achieved.

Using Eq. [2.5] and Eq. [2.6], one can find the maximum allowed angle for the total internal reflection condition.

$$\theta_{max} = n_1\cos\theta_c = \left(n_1^2 - n_2^2\right)^{\frac{1}{2}} \qquad \text{(EQ 2.8)}$$

2.1.2 Dielectric Waveguides

By inserting a layer of material which contains a higher refractive index than the substrate and the upper cladding, on the substrate surface, light can be trapped inside the film by total internal reflection. A rectangular dielectric waveguide will trap light in both the horizontal and vertical directions, providing modal confinement. Figure 2.5 provides a pictorial example of a rectangular dielectric waveguide and a simulated mode profile.

FIGURE 2.5   Example of a dielectric waveguide (a). Simulated mode profile (b) [4]

(a)   **(b)**
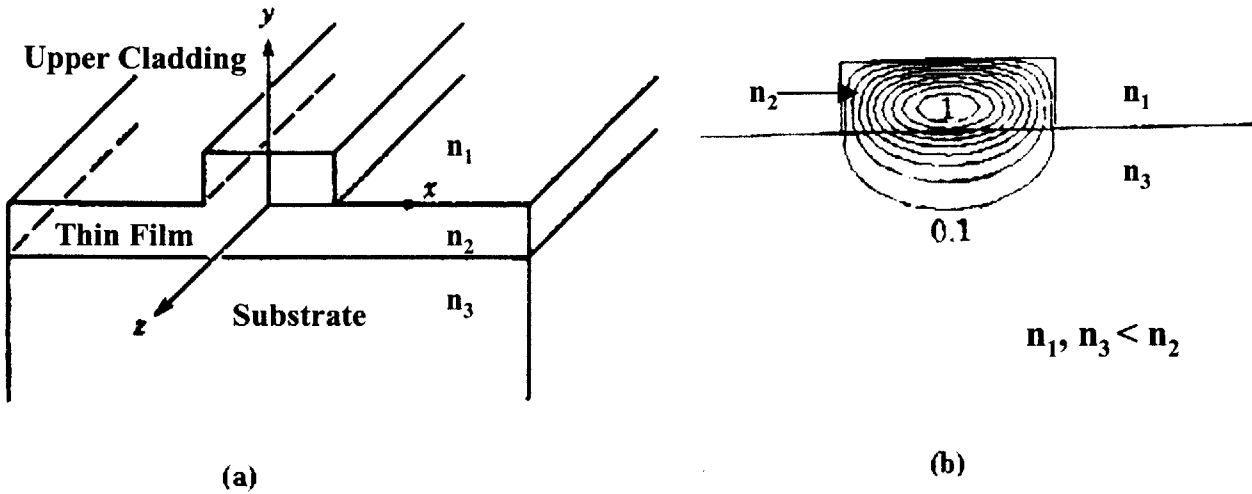
In multi-layered dielectric waveguides, special attention must be given to the effective index of refraction of the guiding layer. The front and side view of a three layer dielectric waveguide are portrayed in Figure 2.6 (a) and (b) respectively.

FIGURE 2.6   Front (a) and side (b) view of a three layer dielectric waveguide [4]

(a)   **(b)**
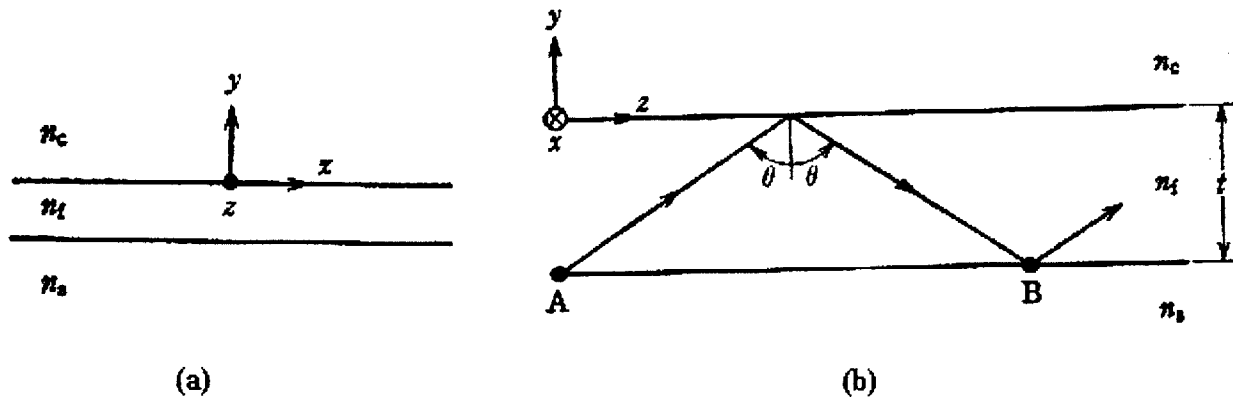
In order for the condition of total internal reflection to be met, the effective index of refraction must be greater than the index of the cladding and substrate. For a

plane wave incident on the dielectric waveguide in Figure 2.6 (b), its phase constant β is given by:

$$\beta = k_o n_f \sin\theta$$

(EQ 2.9)

Where the effective index, n_{eff}, is given by:

$$n_{eff} \equiv \frac{\beta}{k_o} = n_f \sin\theta$$

(EQ 2.10)

The critical angles at the guiding layer substrate surface and the guiding layer cladding surface, can be derived using Eq [2.7]:

$$\theta_{substrate} = arc\sin\left(\frac{n_s}{n_f}\right)$$

(EQ 2.11)

$$\theta_{cladding} = arc\sin\left(\frac{n_c}{n_f}\right)$$

(EQ 2.12)

In order for the total internal reflection condition to be met, $n_c <$ or $= n_s < n_f$ must be satisfied, therefore the effective index of the guiding layer must be greater than that of the substrate and cladding layers.

2.2 Survey of Past Work

2.2.1 Waveguide Bend Fabrication

A significant effort has been put forth in the design of waveguide bends. A number of researchers have examined methods for creating low loss waveguide bends. M. Austin has fabricated rib waveguides on GaAs/Ga$_{0.82}$Al$_{0.18}$As and GaAs/Ga$_{0.92}$Al$_{0.08}$As slices grown by Metal Organic Chemical Vapor Deposition (MO-CVD) [5]. The waveguides were 3μm wide and contained 90° bends with 75, 100, 125, 150, 200, 250, 300, and 400 μm radii. Figure 2.7 displays a schematic of the rib waveguide designed and fabricated by M. Austin.

Austin discovered that minimizing the bending loss while reducing the radius of curvature, could be achieved by creating waveguides with large rib heights. The larger rib heights, predominately surrounded by air, increased lateral confinement. Reducing the height of the slab adjacent to the rib structure was also found to

increase the lateral confinement as well as reduce the number of allowable modes. Insertion losses were also found to be smaller for guides with larger rib heights.

FIGURE 2.7   Rib waveguide designed and fabricated by M. Austin [5]

W = Rib width

H_R = Rib height

H_L = Height of layer adjacent to the rib
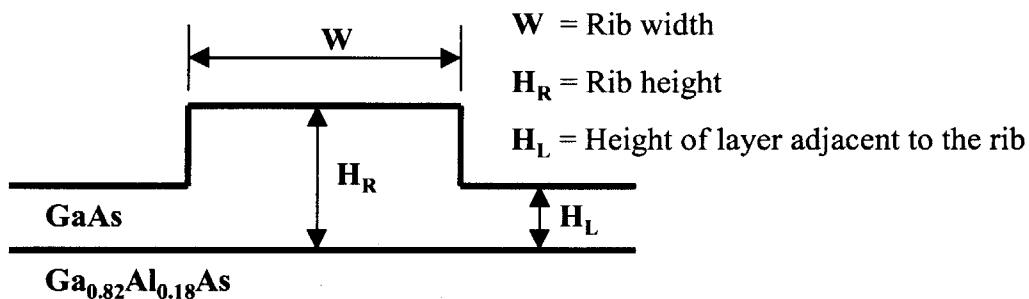
Optical measurements were performed in order to calculate loss. Bending losses were found by dividing the incident optical power by the output optical power, while taking into consideration reflection losses, input coupling efficiency and scattering from the straight waveguide sections. Austin showed that in his case, a minimum loss (approximately 3 dB) for multimode guides bending at 90° occurred when a radius of curvature was 300μm. An 8.5 dB minimum loss was achieved for a single-mode curved guide with a radius of curvature of 400 μm. Austin noted more work was needed with guides of different geometries, material composition and waveguides thicknesses to determine the limiting loss mechanisms.

2.2.2   Waveguide Bend & Offset Simulation

Rajarajan, et al, made use of various numerical methods along with variations of waveguide parameters to simulate waveguide bends [6]. Offsets, Figure 2.8, were used as a means of reducing the loss. In a curved waveguide, the mode profile shifts to the outer edge of the bend which causes a field mismatch at the junction between a straight and bend waveguide. An offset will improve the coupling between the straight and bent sections of the waveguide.

A vectorial finite element-based beam propagation method was used to find the radiation losses and the changes in the mode profile along the waveguide bends. A least squares boundary residual method (LSBR) is used to find the transmission and reflection coefficients at the straight-to-bent waveguide junctions and for off-set optimizations. The initial waveguide, that was used for the numerical simulations, consisted of a GaAs guiding layer placed on a thick 7μm layer of $Al_{0.15}Ga_{0.85}As$. The height and width of the rib were 0.4μm and 3μm respectively. The waveguides also contain an epilayer, a layer above the substrate and

An example of an offset between the straight and bend sections of a waveguide
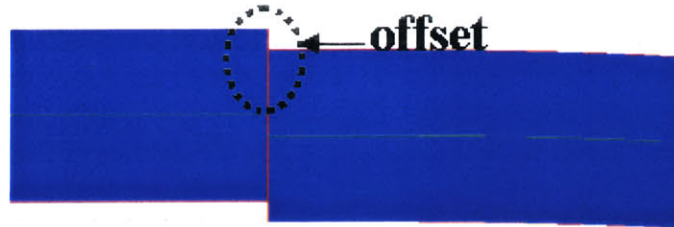
below the rib structure, of 0.4µm. At the simulation wavelength of 1.15µm, the refractive indices of the GaAs and AlGaAs are 3.44 and 3.35 respectively. The waveguides contained 90° bends with a radius of 100µm. Figure 2.9 contains of schematic of the waveguide design.

Rib waveguide designed by Rajarajan, et al [6]
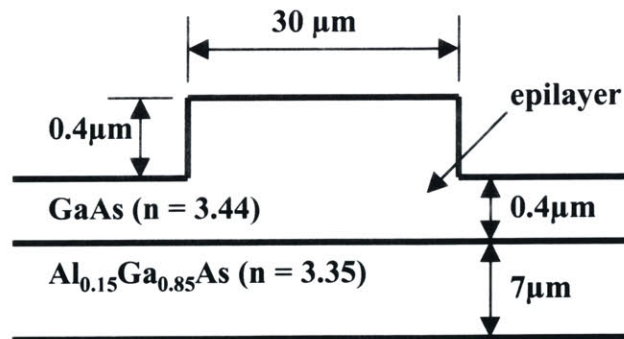
The simulations with the initial parameters showed a loss of 16 dB/90°. A minimum loss value was found to be 1dB/90° for a waveguide with a radius of 275µm. Although the increase in bending radius greatly reduced the loss, tighter bends are much more desired. It was found that reducing the epilayer thickness resulted in the center of the optical mode moving further upwards, radiating less to the outer slab layer, therefore decreasing the loss. Decreasing the epilayer from 0.4µm to 0.3µm lead to a reduced loss of 10 dB/90°. It was noted that completely removing the epilayer would enable the design of low loss compact waveguide bends. For radii of 150µm and 200µm, the bending loss was found to be a minimum with a rib width of 1.9µm. The waveguide became multimode when the rib width was increased beyond 1.85µm. Initial simulations showed the center of the mode profile shifted to the right by more than 1µm after the bend. The transition loss with the initial parameters was found to be 6.5 dB. An offset of 1.3µm provided a min-

imum transition loss of 2.2 dB. Introducing offsets not only reduced the transition loss but also reduced the reflection coefficient as well. The required offset for both TE and TM polarizations were found to be almost identical down to a bending radius of 400μm. For radii smaller than 400μm, the required offsets increased linearly.

Seo, et al, have also investigated losses in waveguide bends with the use of numerical simulations [7]. In addition to offsets, the researchers used isolation trenches next to the waveguide structure as a means of reducing transmission losses. Placing a trench outside the curved waveguide prevents light from spreading outward toward larger radii, thus improving beam confinement.

A 3-D semivectorial finite difference beam propagation program was used for the simulations. Simulations provided the following optimal values; rib height and width of 1.4μm and 2.4μm respectively, offset of 0.5μm, trench distance and width of 2μm and 4μm respectively and an epilayer thickness of 0.4μm. The simulations were calculated on a GaAs/GaAlAs structure with a bending radius of 1.5mm and a propagation wavelength of 1.5μm.

All of the optimizations were calculated with a rib height of 1.4μm, although it was noted a further reduction of transmission loss could be achieved by increasing the height of the rib. Higher rib heights increase the effective index of the rib so that more light is confined by the rib. Simulations found an asymmetric mode in the curved waveguide section and a symmetric mode in the straight waveguide section. A solution to the modal symmetry program was found by sloping the rib walls. The authors proposed having different slopes for the right and left side walls for the rib, stating that the asymmetry in the rib will counter the asymmetry in the bend. It was noted that fabrication of such a configuration would be hard to obtain. Placing the sample at an angle during the etching process was suggested to obtain the asymmetry in the bend.

2.2.3 Total Internal Reflection Bend

C. Manolatou et al [8] used the concept and design of total internal reflection to design compact waveguide bends. Manolatou et al discovered the performance of sharp 90° bends in high contrast, single mode waveguides could be enhanced with the placement of a resonant cavity at the corner of the guide. The radiation loss, due to the mode mismatch at the corner of the bends, was reduced by achieving strong coupling of the waveguide modes to the resonator modes. Figure 2.10 shows the simulated electric field amplitude results of transmission through a sharp 90° bend. A great amount of radiation loss was incurred as light transversed through the bend.

FIGURE 2.10   (a) Schematic of a sharp 90° bend. (b) Electric field amplitude in the bend.[8]

$n_i = 3.2$

$n_o = 1$

$w = 0.2 \ \mu m$

(a)   (b)
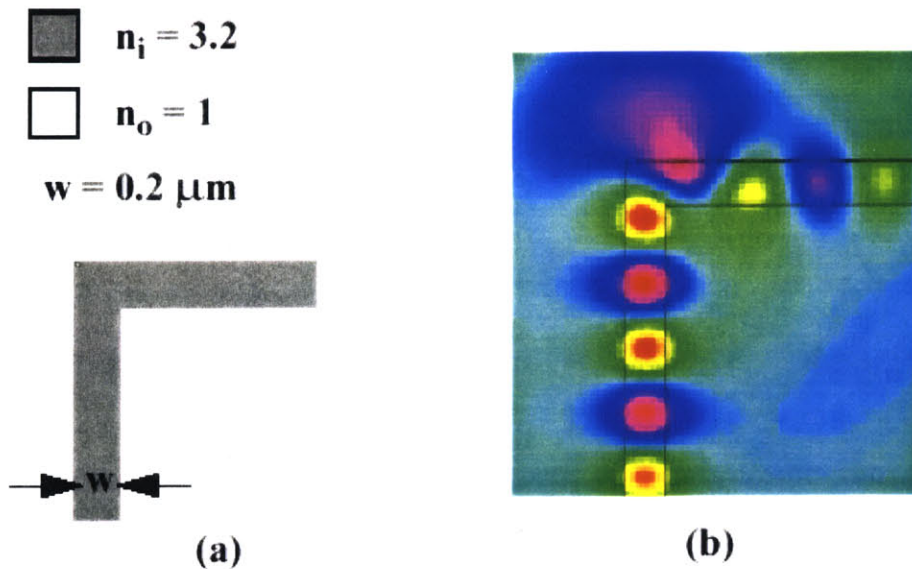
A first attempt of placing a resonant cavity at the corner of the guide, was done by increasing the volume of the dielectric at the corner region to form a square resonator. Figure 2.11 displays the simulated results. The electric field pattern shows a great reduction of the radiation loss but poor transmission was detected and reported with the use of other simulation programs. In order to further improve the bend, the coupling between the cavity and the waveguide mode relative to the coupling radiation, was increased. The increase in coupling was achieved by pushing the cavity mode at the corner region inwards in order to obtain better mode matching. The waveguide bend, shown in Figure 2.12, depicts a waveguide with the improvements mentioned above, in which a cut on the corner of the waveguide was used to produce the desired effects. The final improvement total internal reflection bends almost completely eliminate the radiation loss while containing a transmission of nearly 99%, as was reported with use of simulation programs.

FIGURE 2.11 (a) Schematic and (b) electric field amplitude of improvement bend. [8]

$n_i = 3.2$ $w = 0.2 \mu m$

$n_o = 1$ $a = 0.62 \mu m$

(a)   **(b)**
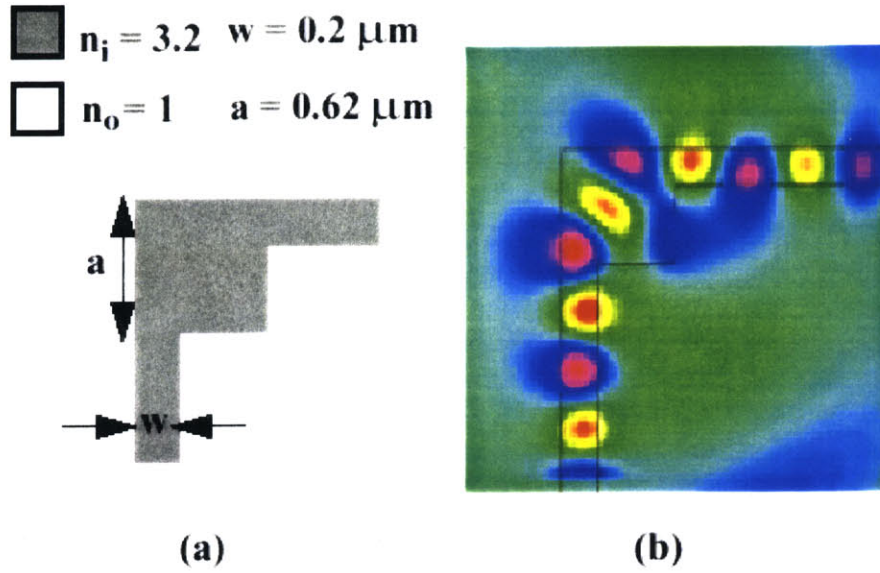
FIGURE 2.12 (a) Schematic and (b) electric field amplitude of the final improvement bend. [8]

$n_i = 3.2$ $w = 0.2 \mu m$

$n_o = 1$ $a = 0.72 \mu m$

(b)

(a)
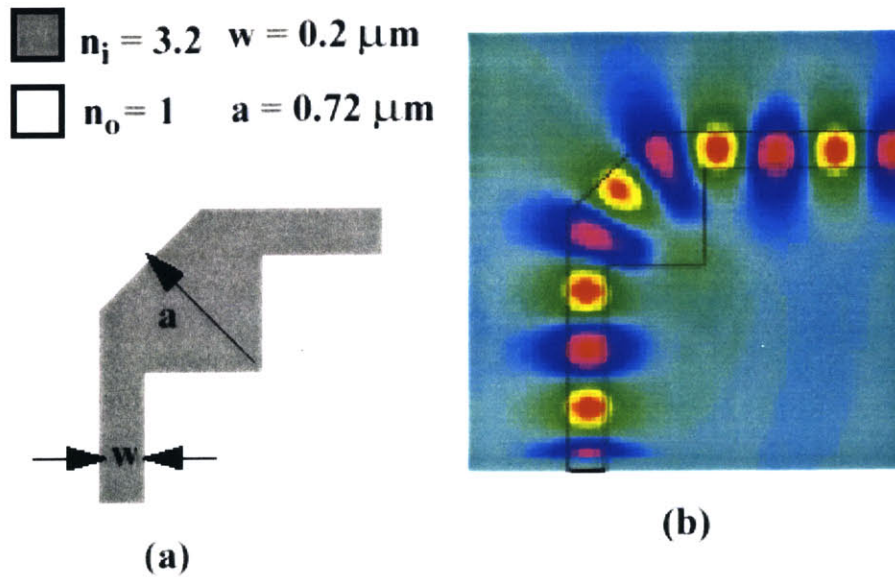
2.3 Design & Simulations

2.3.1 Straight Waveguide Simulation

The goal is to fabricate and test waveguide bends in the (In,Ga)(As,P) material system. For use in photonic integrated circuits, $In_{1-x}Ga_xAs_yP_{1-y}$ lattice matched to InP offers a bandgap range which is compatible with optical fiber networks. In order to achieve a single mode waveguide with good mode confinement, the effective index of the passive waveguide should be above InP (n=3.167) but well below that of the active material (n=3.424). A waveguide with a low effective index may be obtained by alternating a quarternary layer ($In_{0.56}Ga_{0.44}As_{0.95}P_{0.07}$, n=3.294) with InP layers. Two different structures have been grown; layer A and layer B. The grown structures differ in the thicknesses for the quaternary and InP layers. The mode profile simulations have been performed on OptiWave, a 3-D mode solving simulation program. Both layer A and layer B were simulated for mode profiles with widths ranging from 1μm to 7μm and a fixed height of 1.5μm. Figure 2.13 through Figure 2.27 are the simulated results for the various straight waveguides, where the mode profile has been calculated for both TE and TM incident waves.

FIGURE 2.13   Waveguide design layer A width = 2μm. TE incident wave
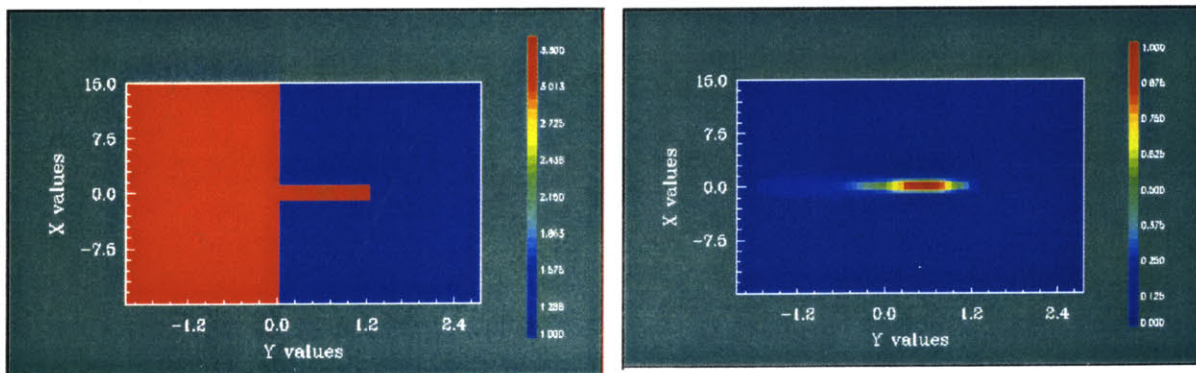
Mode Order: 0
Modal Index: 3.172

FIGURE 2.14 Waveguide design layer A width = 2µm. TM incident wave

Mode Order: 0
Modal Index: 3.172
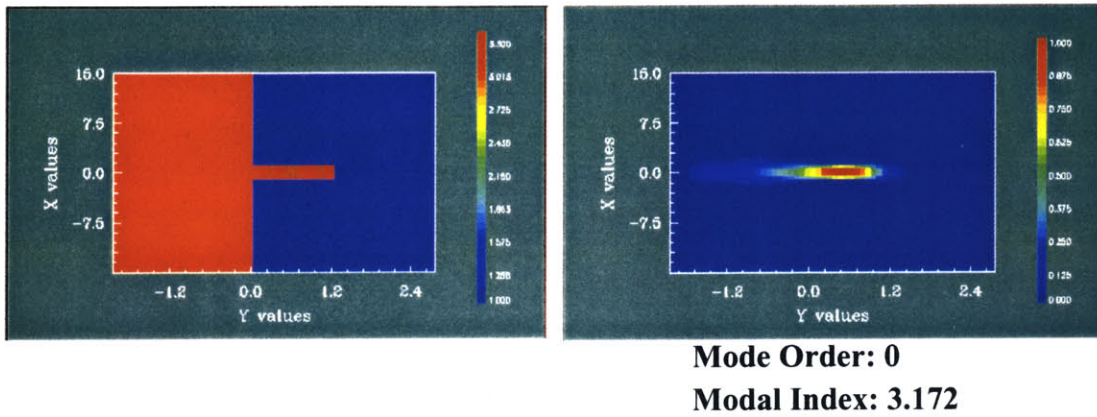
FIGURE 2.15 Waveguide design layer A width = 3µm. TE incident wave

Mode Order: 0
Modal Index: 3.182
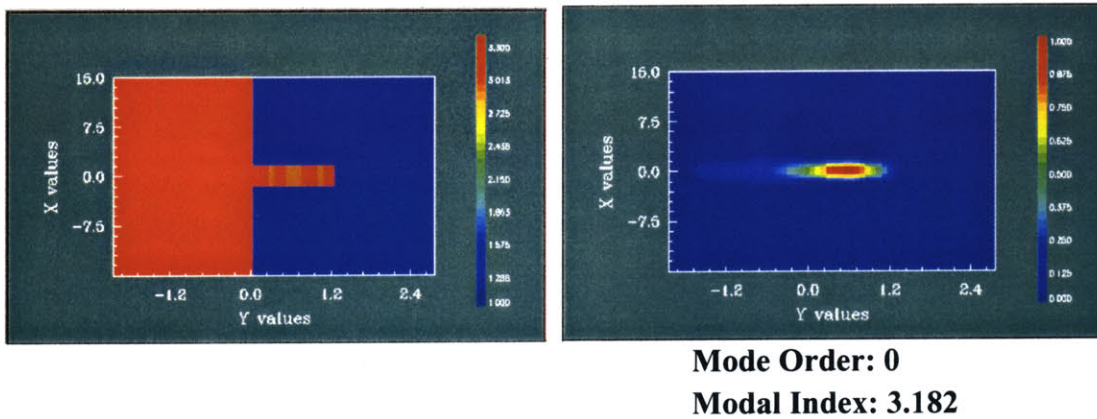
FIGURE 2.16 Waveguide design layer A width = 3µm. TM incident wave

Mode Order: 0
Modal Index: 3.179
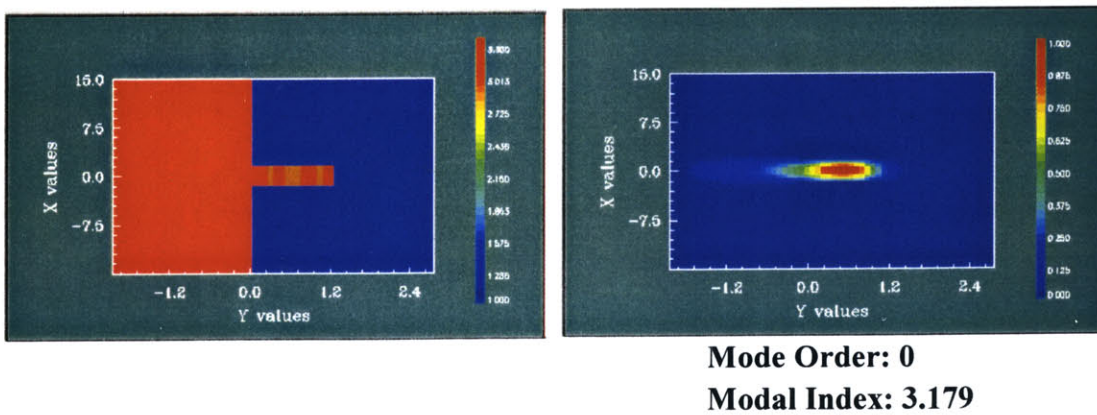
FIGURE 2.17   Waveguide design layer A width = 4µm. TE incident wave

Mode Order: 0   **Mode Order: 1**
Modal Index: 3.186   **Modal Index: 3.171**
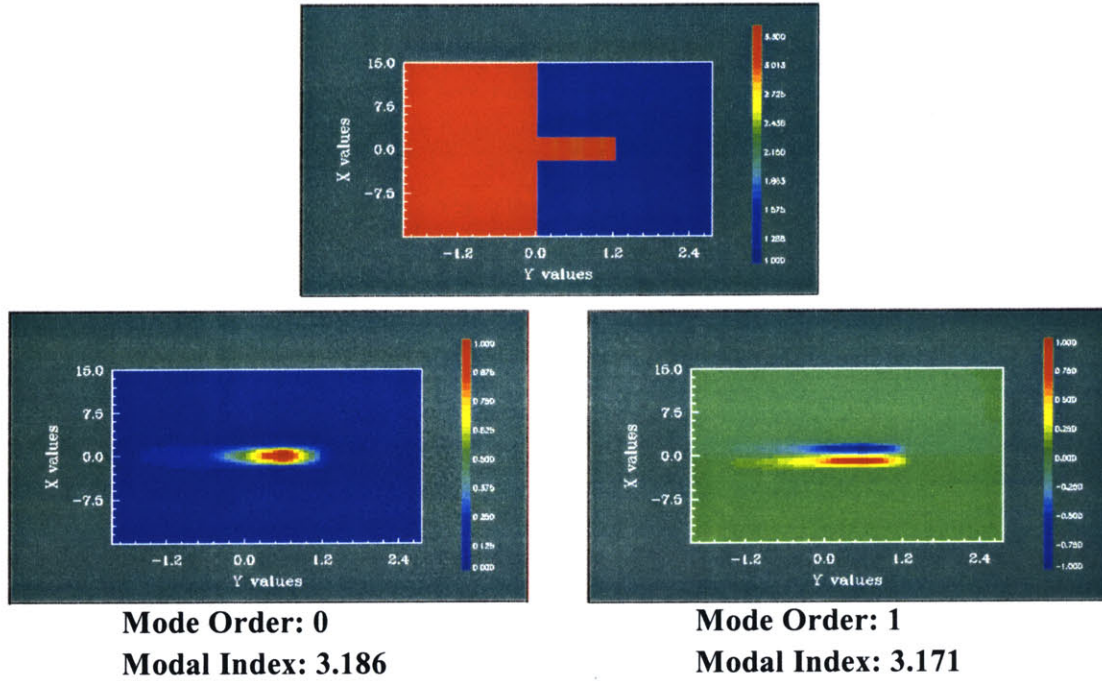
FIGURE 2.18   Waveguide design layer A width = 4µm. TM incident wave

Mode Order: 0   **Mode Order: 1**
Modal Index: 3.181   **Modal Index: 3.169**
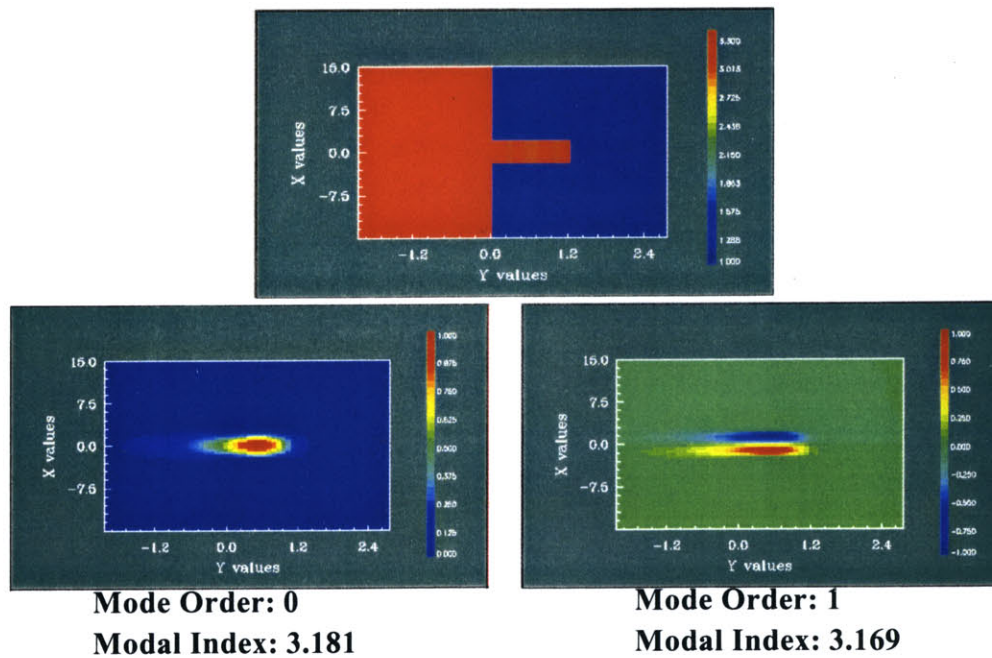
FIGURE 2.19   Waveguide design layer A width = 5µm. TE incident wave

Mode Order: 0
Modal Index: 3.188

Mode Order: 1
Modal Index: 3.178
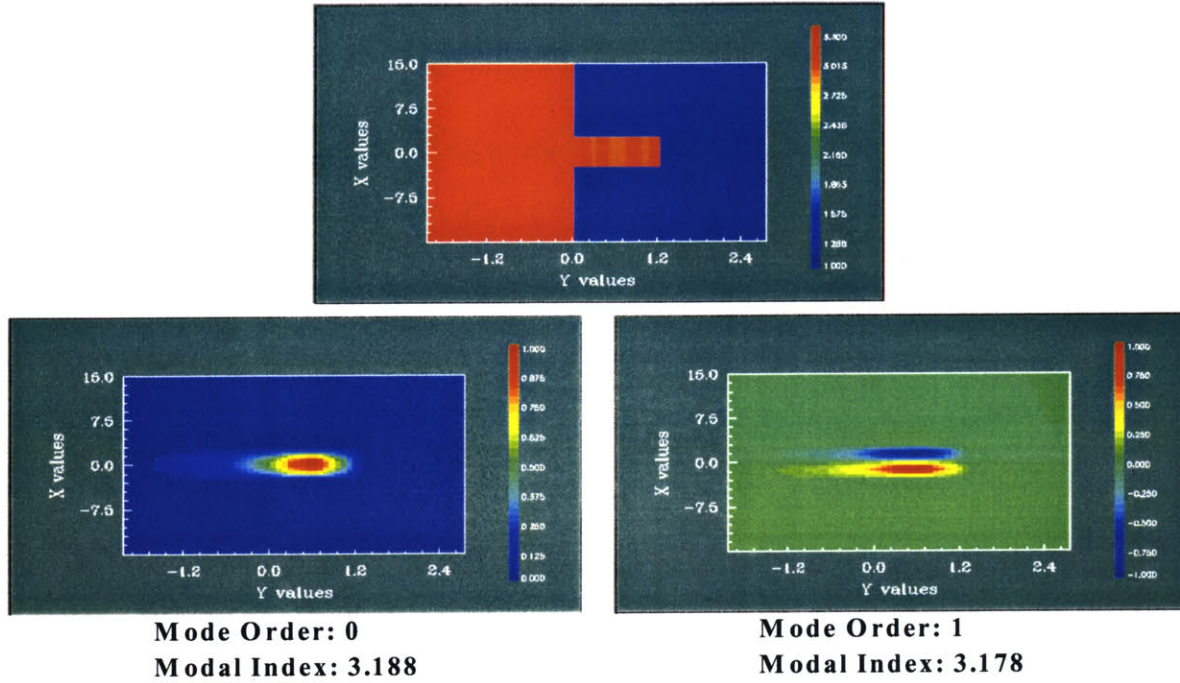
FIGURE 2.20   Waveguide design layer A width = 5µm. TM incident wave

Mode Order: 0
Modal Index: 3.183

Mode Order: 1
Modal Index: 3.174
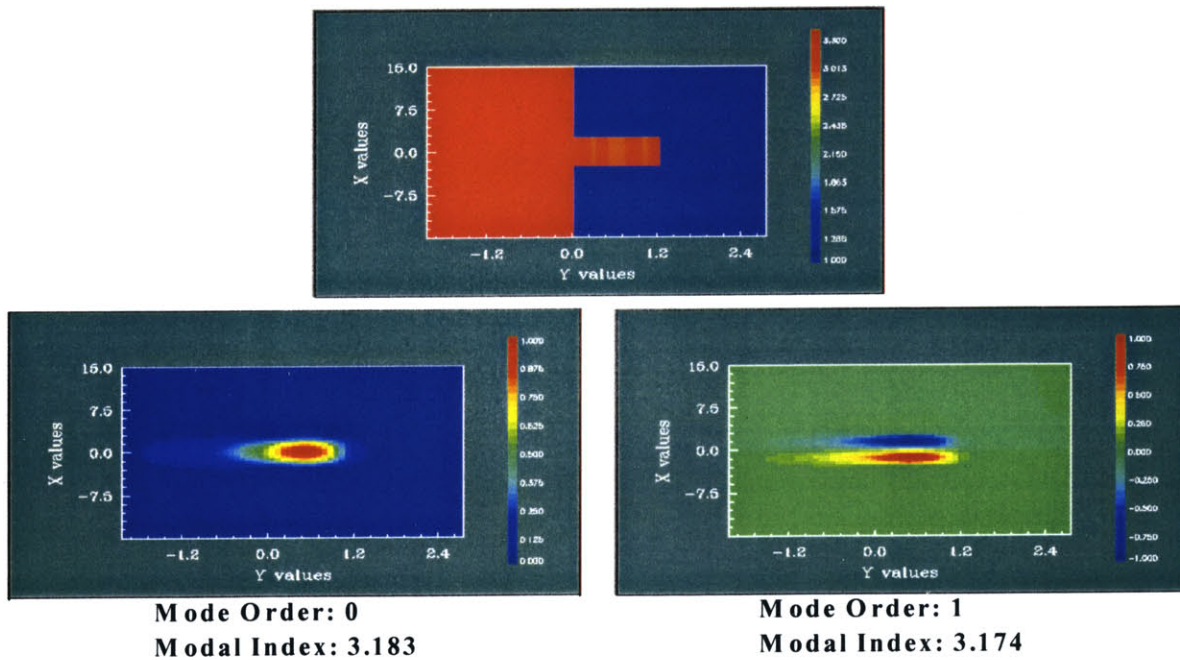
FIGURE 2.21   Waveguide design layer A width = 6μm. TE incident wave

Mode Order: 0
Modal Index: 3.188

Mode Order: 1
Modal Index: 3.182

Mode Order: 2
Modal Index: 3.170
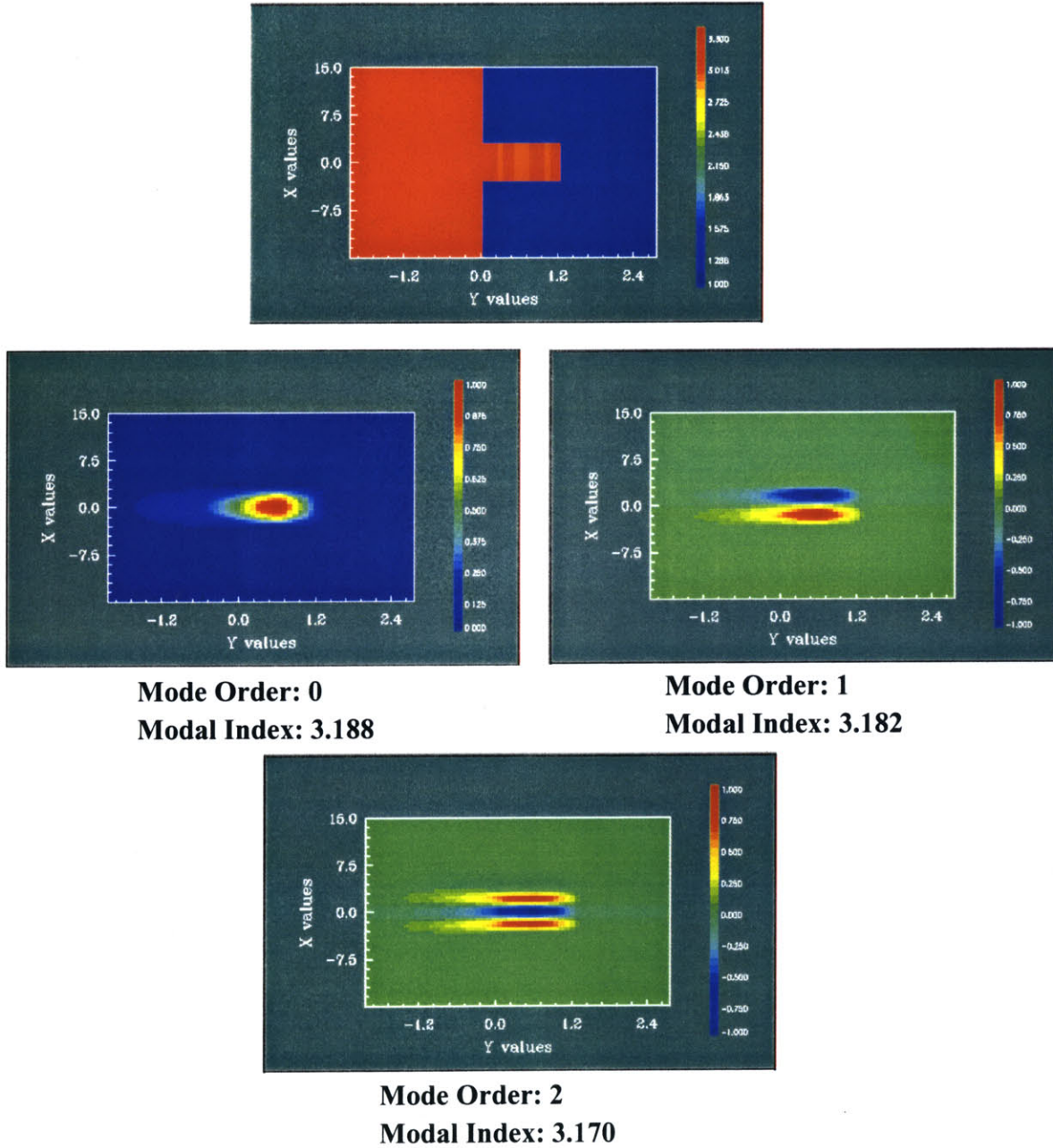
FIGURE 2.22   Waveguide design layer A width = 6μm. TM incident wave

Mode Order: 0
Modal Index: 3.183

Mode Order: 1
Modal Index: 3.177

Mode Order: 2
Modal Index: 3.167
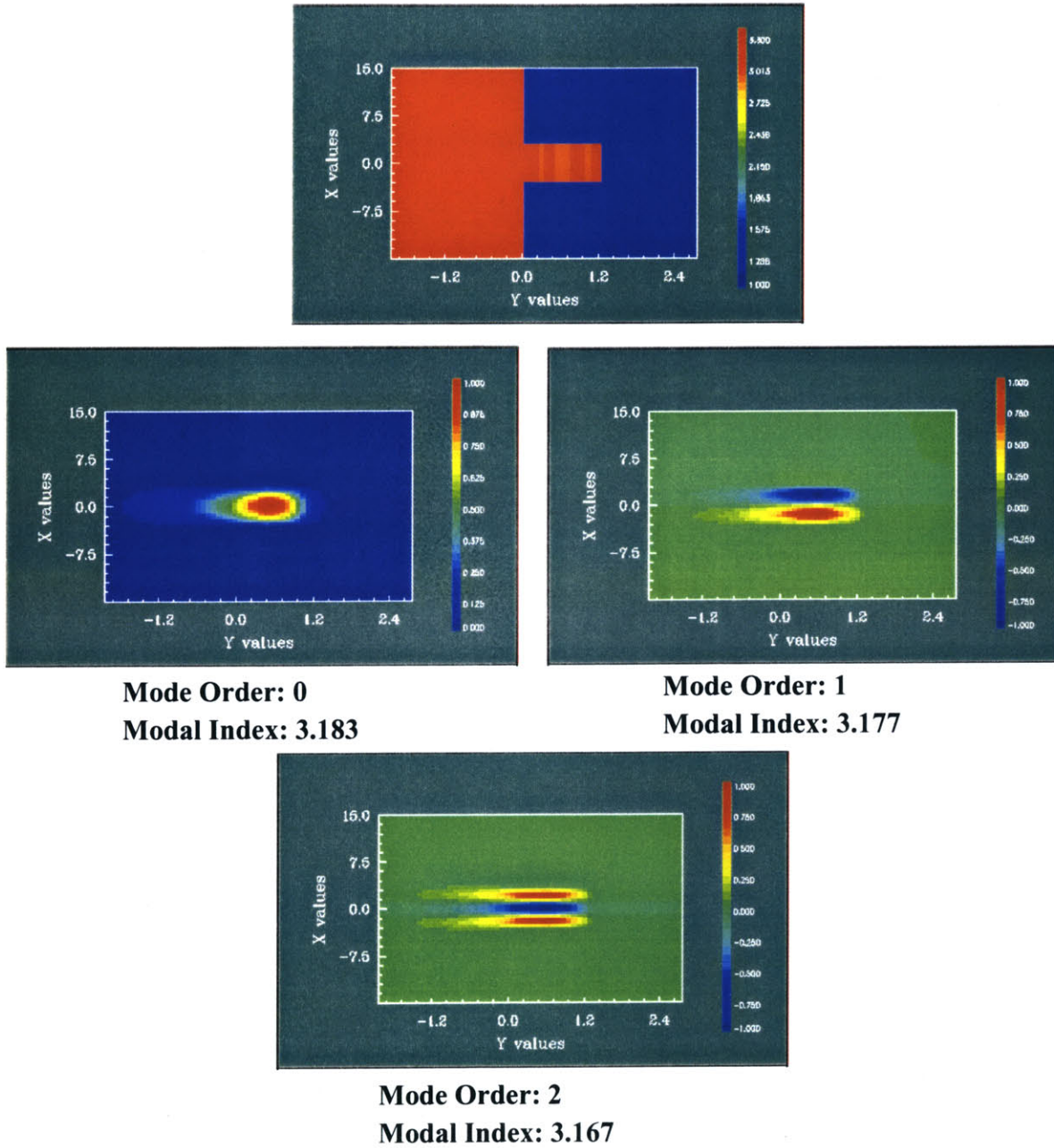
FIGURE 2.23   Waveguide design layer A width = 7µm. TE incident wave.

Mode Order: 0
Modal Index: 3.189

Mode Order: 1
Modal Index: 3.184

Mode Order: 2
Modal Index: 3.176
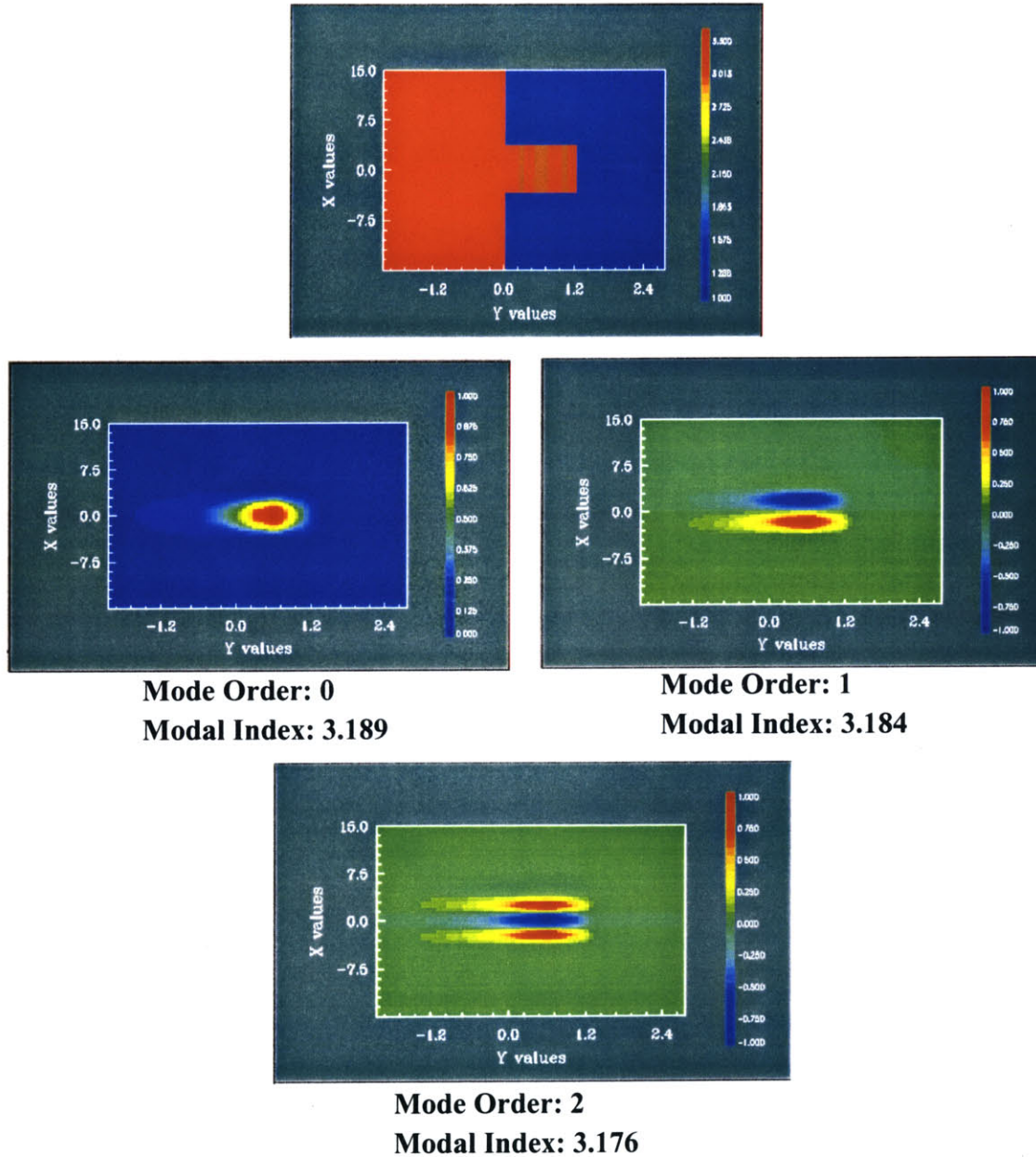
FIGURE 2.24 Waveguide design layer A width = 7μm. TM incident wave

Mode Order: 0
Modal Index: 3.184

Mode Order: 1
Modal Index: 3.179

Mode Order: 2
Modal Index: 3.172
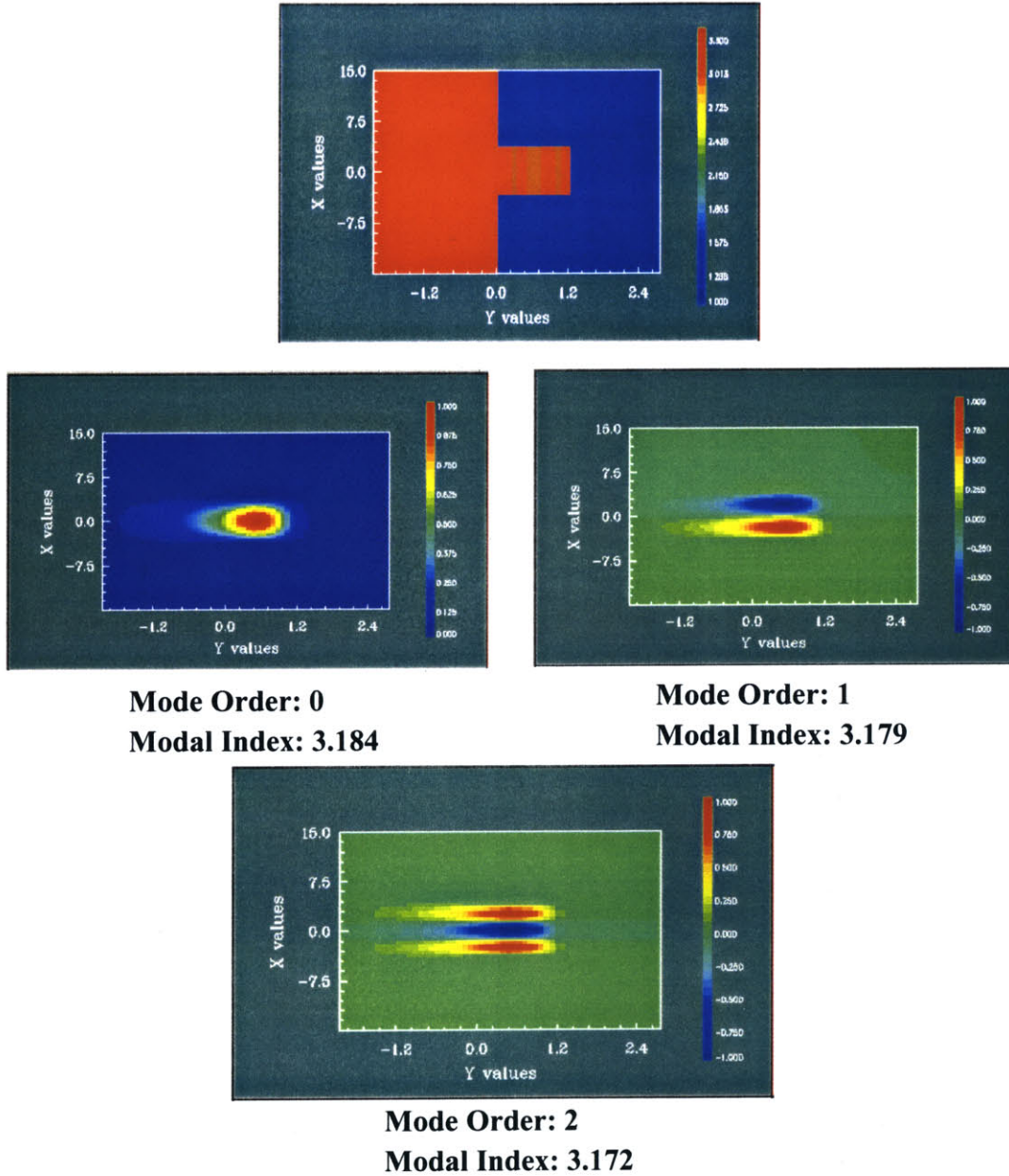
FIGURE 2.25   Waveguide design layer B width = 5µm. TE incident wave

Mode Order: 0
Modal Index: 3.168
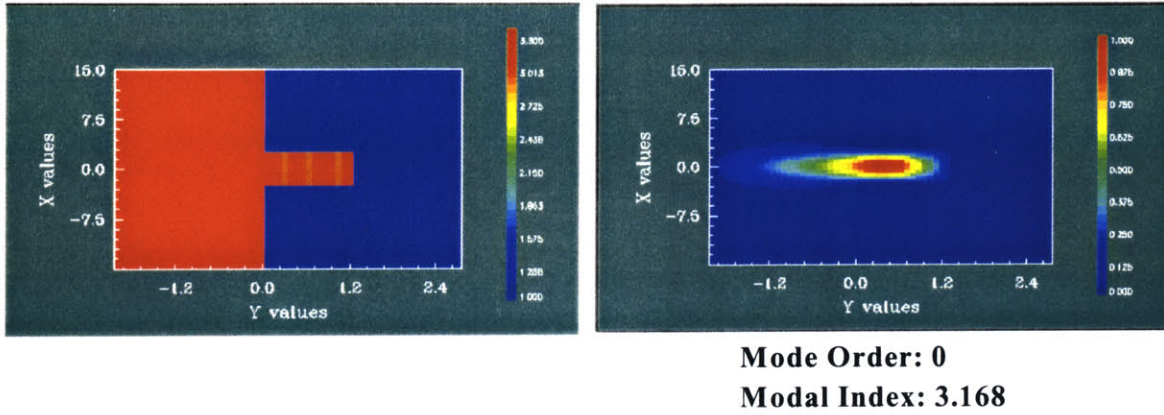
FIGURE 2.26   Waveguide design layer B width = 6µm. TE incident wave

Mode Order: 0
Modal Index: 3.169
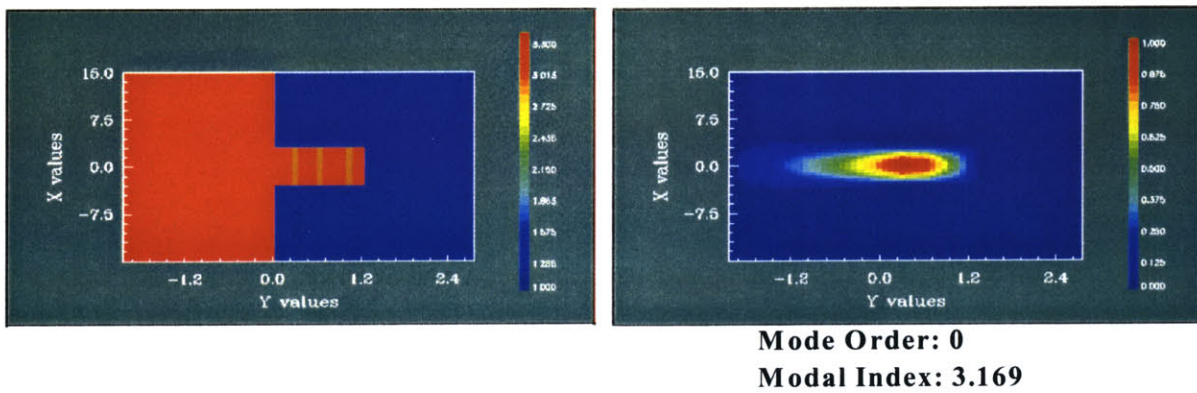
FIGURE 2.27   Waveguide design layer B width = 7µm. TE incident wave

Mode Order: 0
Modal Index: 3.169
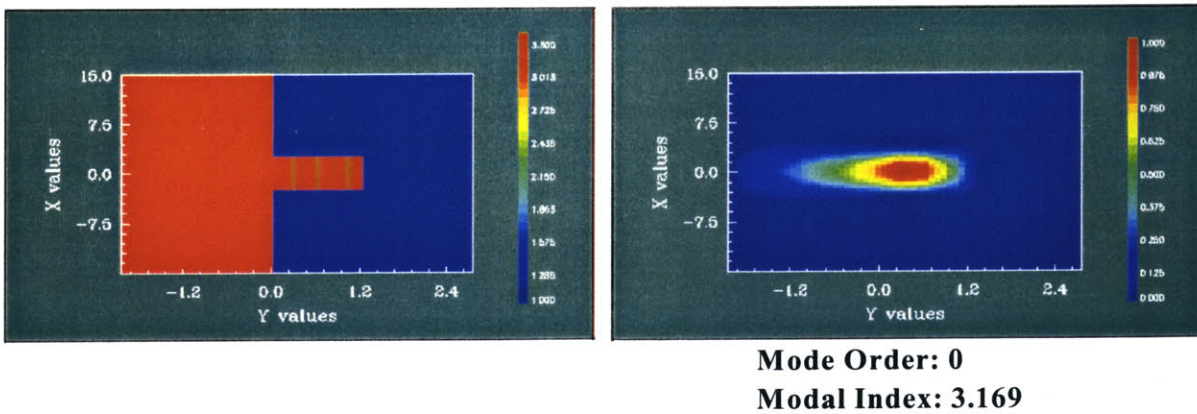
The 1μm wide waveguides for both layer A and layer B were not capable of confining the mode. The mode solver therefore did not find modes for the 1μm wide waveguides. There were also no modes found for layer B waveguide widths of 1μm, 2μm, 3μm and 4μm. The simulation program also gave single mode results for layer B waveguide widths of 7μm, 6μm and 5μm. These results are unlikely, future work should be done with optimizing the number of points in the mode solving calculation in order to achieve more believable results. All of the simulated results were in agreement with the TE modal indices being higher than its corresponding TM index. The greater the index of the waveguide, the greater the modal confinement. Therefore, the simulated results suggest the waveguides will be less lossy with TE incident waves, which is expected. Single mode results for layer A were found with waveguides widths 2μm and 3μm. Simulated results will be compared with experimental measurements.

2.3.2 Mask Design

In order to obtain a substantial range of data for the loss measurements, a number of waveguides have been fabricated varying in width and bending radius. Eight different sine s-bends have been fabricated, with use of an OptiWave waveguide modeling software program, with varying vertical and horizontal displacements, show in Figure 2.28. Radii for the various bends have been determined by mapping a cosine wave with similar displacement values, to a circle. The horizontal displacements shown are approximately 5% shorter than the displacement values given by the software program, as a result of a small straight waveguide section place and the start and end of each sine s-bend section.

FIGURE 2.28   Example of Sine S-bend showing vertical and horizontal displacements
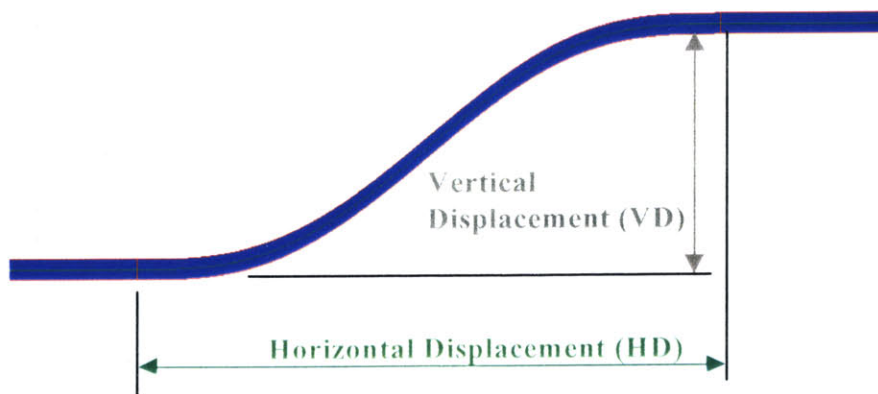
The displacement and approximate radii values for the sine s-bends are as follows:

Sine S-bend Number	Vertical Displacement (μm)	Horizontal Displacement (μm)	Radius (μm)
(1)	60	190	179.86
(2)	75	150	142.53
(3)	53	115.75	109.32
(4)	167.5	380	365.59
(5)	98	470	448.66
(6)	80	265	252.14
(7)	66.25	132.5	127.69
(8)	385	802.5	779.46

The bends have been separated in two sets. Set A contains s-bends (1) - (4) as described below. Set B contains s-bends (5) - (8) as described below. SWG is short hand notation for straight waveguide. Each of the bends are separated by straight sections on the waveguide. Sets A and B are laid out from top to bottom as follows:

Set A:

Waveguide Type	Radius (μm)	Number of Sine S-Bends
SWG	N/A	N/A
S-bend (1)	179.86	4
SWG	N/A	N/A
S-bend (1)	179.86	6
SWG	N/A	N/A
S-bend (1)	179.86	2
SWG	N/A	N/A
S-bend (2)	142.53	6
SWG	N/A	N/A
S-bend (2)	142.53	4
SWG	N/A	N/A
S-bend (2)	142.53	2
SWG	N/A	N/A
S-bend (3)	109.32	4
SWG	N/A	N/A
S-bend (3)	109.32	6
SWG	N/A	N/A
S-bend (3)	109.32	2
SWG	N/A	N/A
S-bend (4)	365.59	4
SWG	N/A	N/A
S-bend (4)	365.59	2
SWG	N/A	N/A

Set B:

Waveguide Type	Radius (μm)	Number of Sine S-Bends
SWG	N/A	N/A
S-bend (5)	448.66	6
SWG	N/A	N/A
S-bend (5)	448.66	4
SWG	N/A	N/A
S-bend (5)	448.66	2
SWG	N/A	N/A
S-bend (6)	252.14	6
SWG	N/A	N/A
S-bend (6)	252.14	4
SWG	N/A	N/A
S-bend (6)	252.14	2
SWG	N/A	N/A
S-bend (7)	127.69	6
SWG	N/A	N/A
S-bend (7)	127.69	4
SWG	N/A	N/A
S-bend (7)	127.69	2
SWG	N/A	N/A
S-bend (8)	779.46	4
SWG	N/A	N/A
S-bend (8)	779.46	2
SWG	N/A	N/A

Both sets A and B were fabricated with waveguide widths ranging from 1µm thorough 7µm. A mask was designed containing seventeen six by six millimeter dies, Figure 2.29. All the dies consist of either set A or B, straight waveguides followed by a set of three identical waveguides containing a number of bends; Figure 2.30 depicts an example of a die.

FIGURE 2.29   The mask layout containing the various dies
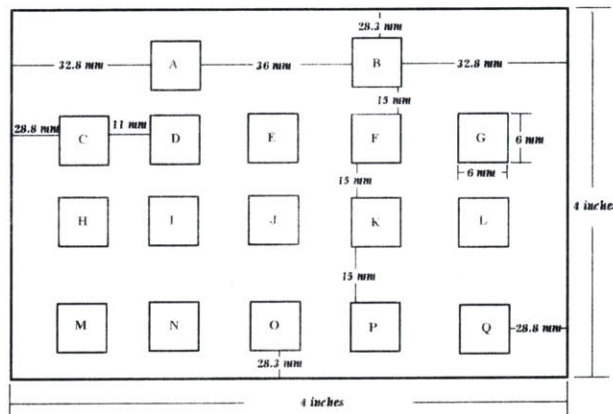
FIGURE 2.30   An example of one of the many dies fabricated, set A

For each bend, there are three duplicates of three identical waveguides. Each duplicate contains a different number of bends. The purpose of this configuration is to ensure the loss measured in the waveguides is linear with the number of bends. Each bend is matched with its mirror image (y-axis), this is to insure that the entry and the exit points lay on the same line, for ease in measuring. Dies C thorough I contain set A with widths 1 thorough 7µm, respectively, and dies J thor-

ough P contain set B with widths 1 thorough 7µm respectively. Die A contains waveguide bends (1) thorough (4) with offsets of 0.2, 0.4 and 0.6µm. Die B contains waveguide bends (5) thorough (8) with offsets of 0.4, 0.4 and 0.6µm. As before, for die A and B, each bend is fabricated in a duplicate of three per offset, each set is followed by a straight waveguide. Die Q contains a set of total internal reflection bends. Figure 2.31 depicts the three different total internal reflection bends with their dimensions. The total internal reflection bends were designed in duplicates of three, various sets contained a different number of bends. Each set was separated by a straight waveguide.

FIGURE 2.31   Total internal reflection bends. (a) Resonator bend. (b) Corner mirror bend. (c) Double corner mirror bend
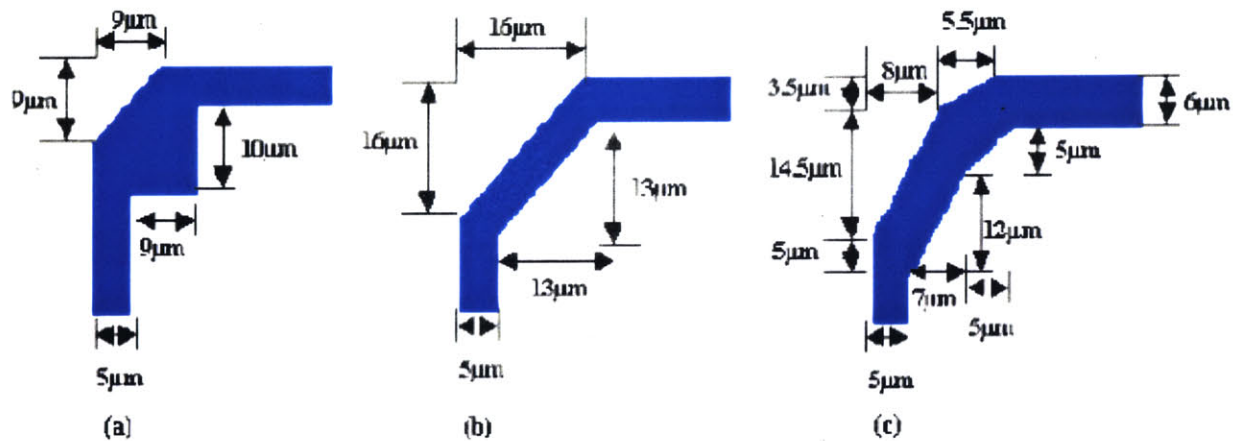
RESEARCH APPROACH

3.0 RESEARCH APPROACH

3.1 Research Objective

The goal is to design and fabricate low loss passive InP waveguide bends. A variety of bending radii and waveguide widths will be tested and measured for loss. The dimensions of an ideal low loss bend are to be found for future use in photonic integrated circuits.

The waveguides will be fabricated in an InGaAsP material system. The dimensions of the waveguide, height and width, will greatly effect the mode profile and the loss in the waveguide. All of the waveguides will have a total height of 1.2μm while the width varies from 1μm to 7μm. Two different structures were grown and will be investigated, layer A and layer B. The waveguides will contain an even number of bends so the entry and exit point of the guide lies on the same plane, for ease of measuring.

3.2 Fabrication Sequence

The following fabrication sequence contains the steps which were taken to fabricate the passive waveguide bends. All of the fabrication was performed in the Nanostructures Laboratory (NSL).

FIGURE 3.32   Gas source molecular epitaxy growth layer A (a) and layer B (b)

(a)

200nm InP
100nm InGaAsP
200nm InP
200nm InGaAsP
200nm InP
100nm InGaAsP
200nm InP
InP Substrate

(b)

200nm InP
100nm InGaAsP
250nm InP
100nm InGaAsP
250nm InP
100nm InGaAsP
200nm InP
InP Substrate
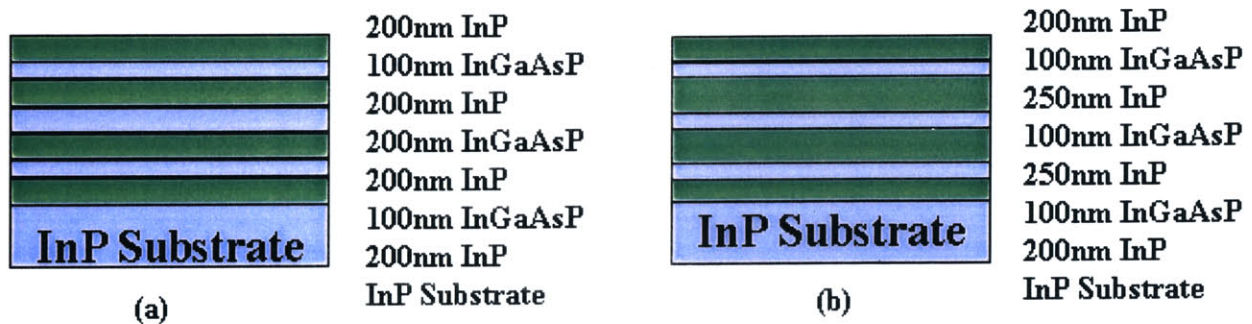
Figure 3.32 shows two grown structures as a result of the gas source molecular beam epitaxy (GSMBE). After the InP wafer contains the grown films on its substrate, the wafer was cleaved into quarters. Figure 3.33 depicts the next step in the process.

39   **Towards Photonic Integrated Circuits**

FIGURE 3.33   Top layer of SiO$_2$ deposited on the epilayer

350nm top layer of SiO$_2$ →

InP substrate
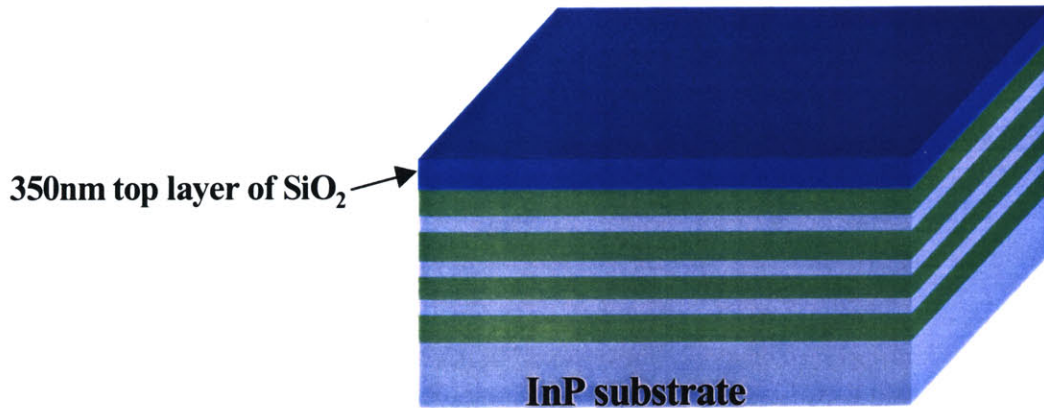
A 350nm layer of SiO$_2$ was deposited with use of a sputter deposition system. SiO$_2$ is used as a hard mask during the etch of the GSMBE-grown structure.

FIGURE 3.34   Photolithography process

1.5µm Photoresist Pattern →

InP substrate
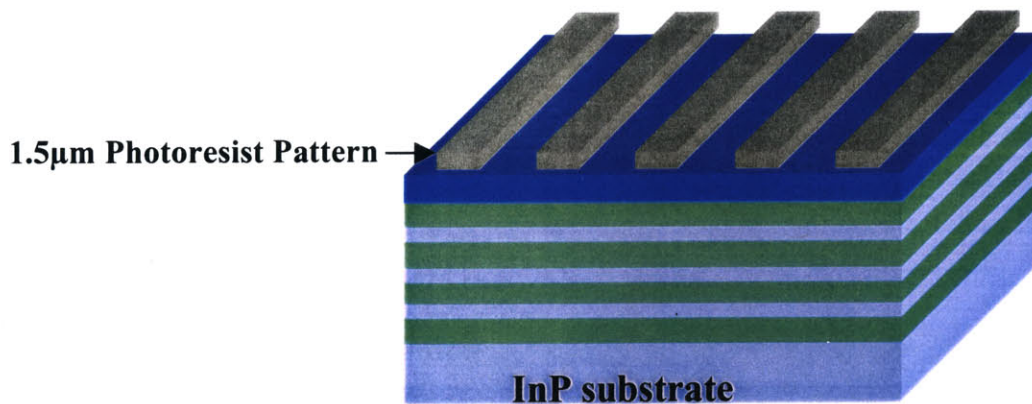
Figure 3.34 shows the results of the photolithography process. The photolithography process is necessary in order to pattern the SiO$_2$ hard mask. The photoresist pattern was used as a mask for etching SiO$_2$.

Figure 3.35 (a) depicts the results of the SiO_2 etch where the photoresist pattern was used as a mask. Notice the same patterns which were formed on the photoresist have been transformed to the SiO_2 layer.

FIGURE 3.35   Results after SiO_2 (a) and Ash (b)
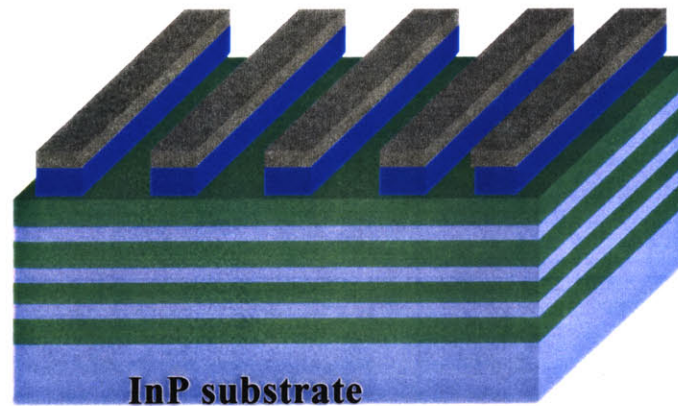
(a)
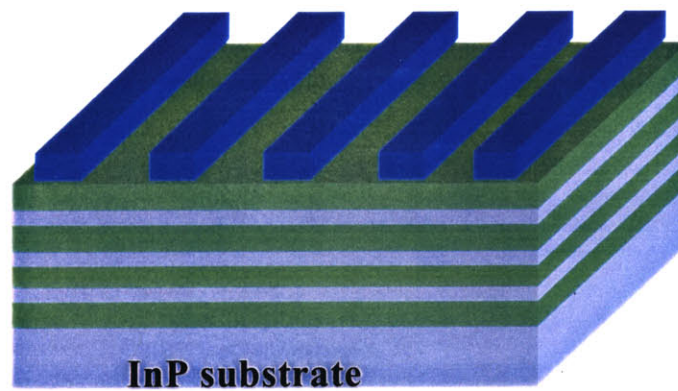
(b)

Figure 3.35 (b) depicts a sample after an ashing step where the photoresist has been stripped away. The SiO_2 pattern is now used as a hard mask for etching in to the InP/InGaAsP layers.

FIGURE 3.36   Results after RIE etching
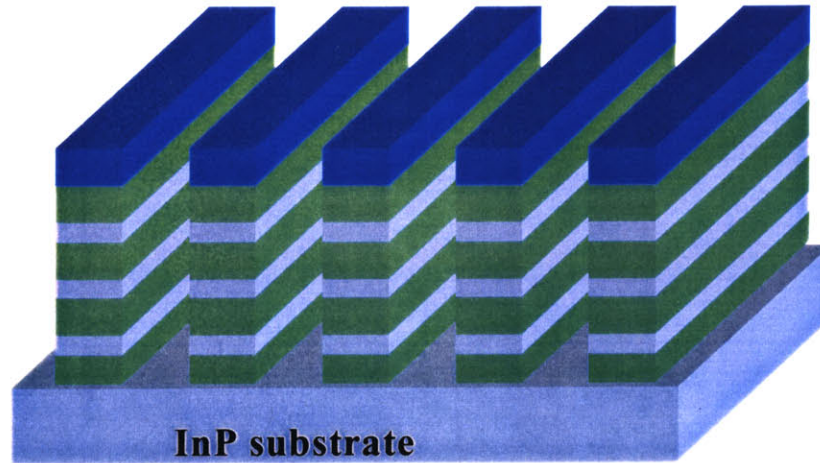
Figure 3.36 shows the final step of the process, where the SiO_2 pattern is used as a hard mask for reactive ion etching (RIE). RIE etches down to the InP/InGaAsP layers stopping at the substrate, for a total of $1.2\mu m$. Since the actually devices will have a top layer of SiO_2, a final SiO_2 etch is omitted.

4.0 FABRICATION DISCUSSION & RESULTS

4.1 Gas Source Molecular Beam Epitaxy Results

Two structures, layer A and layer B, were grown using the Riber Instruments gas source molecular beam epitaxy system. Molecular beam epitaxy is a thin film deposition technique capable of controlling layer thickness and composition precisely and of growing uniform ultra thin layers with abrupt interfaces [9]. Figure 4.37 displays the dimensions of the grown structures.

FIGURE 4.37 MBE grown structures layer A (a) and layer B (b)
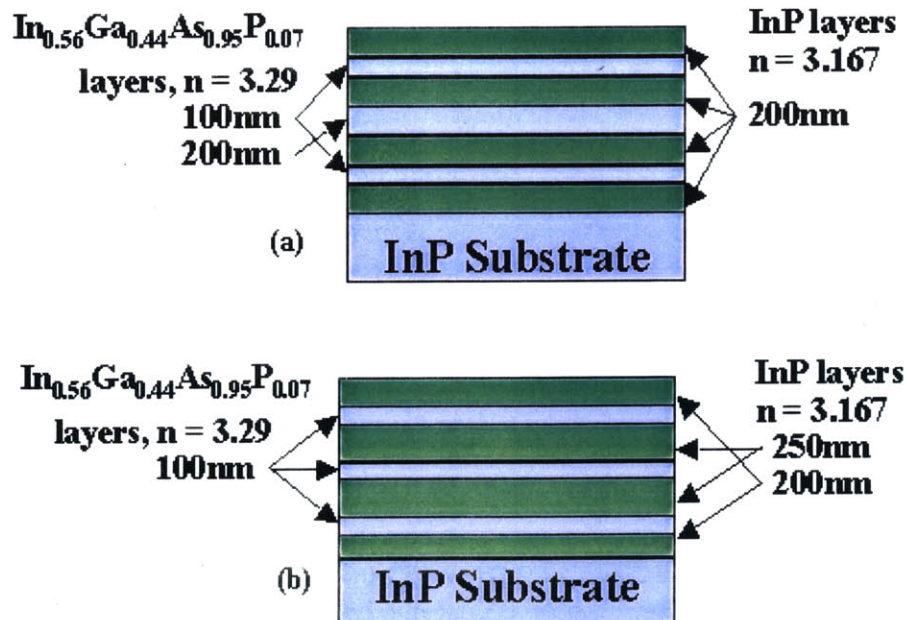
The quarternary $In_{0.56}Ga_{0.44}As_{0.95}P_{0.07}$ layers were used for the purpose of raising the effective index of the guiding layer, so that the guiding layer contains an effective index higher than the InP substrate and the top cladding layer. The growth process was performed on whole wafers, which were later cleaved to quarter wafers for further fabrication.

4.2 Photolithography Results

Photolithography is used to transfer the waveguide images via a photo-mask, Figure 2.29 and Figure 2.30, to the substrate. The first step in the photolithography process is to deposit approximately 350nm of SiO_2 on quarter wafer samples, using a sputtering system. Figure 4.38 depicts the results of a sample having undergone the SiO_2 deposition process. SiO_2 is used as a hard mask in plasma etches which take place later on in the process flow.
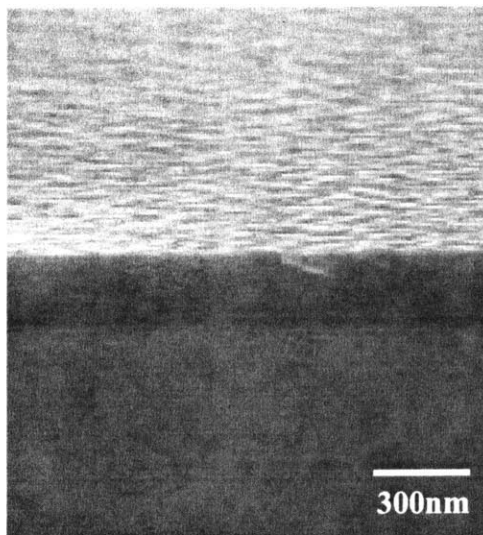
FIGURE 4.38   Scanning electron microscope image (SEM) of a 350nm thick SiO_2 layer used as a hard mask in future fabrication steps

Following the SiO_2 deposition, Hexa Methyl Di Silazane (HMDS) and photoresist are spun on the sample and then baked. HMDS is typically used in the semiconductor industry, to improve the adhesion of photoresist to oxides by reacting with both the oxide and resist surfaces. The HMDS was applied to the wafer, left to sit for 30 seconds and then spun for 1 minute at 3000rpm. The photo-mask was designed for the use of a positive photoresist, therefore 1813 resist was used. An approximately 1.5 μm layer of 1813 resist was spun on the sample at 3000rpm for 1 minute. The spin was followed by a 30 minute bake in an oven with a temperature of 90°C. Contact exposure was performed using a Tamarack UV exposure system. Shipley 352 developer was used in the final development stage of the photolithography process.

4.2.1 Photolithography Problems & Solutions

Initially, the quarter wafer sample were first cleaved into five 7mm square samples prior to spinning the resist. This caused a build up of resist on the edge of each sample. Acetone was used as a failed attempt at removing this edge bead. Because of the resist edge bead, complete contact could not be made between the photo-mask and sample. The appearance of Newton rings resulted from the poor contact and allowed the transfer of undesired patterns unto the sample. Figure 4.39 is a SEM image showing the formed patterns. A trench along the sidewall of the waveguides also resulted, depicted in Figure 4.40. Spinning and baking the resist on the quarter wafer sample before cleaving the sample, resulted in better contact and eliminated the Newton rings. Two scrap SiO_2 half wafer pieces were placed to the left and right of the sample to improve the leveling of the photo-mask over the sample.

FIGURE 4.39   Pattern due to poor contact during UV exposure
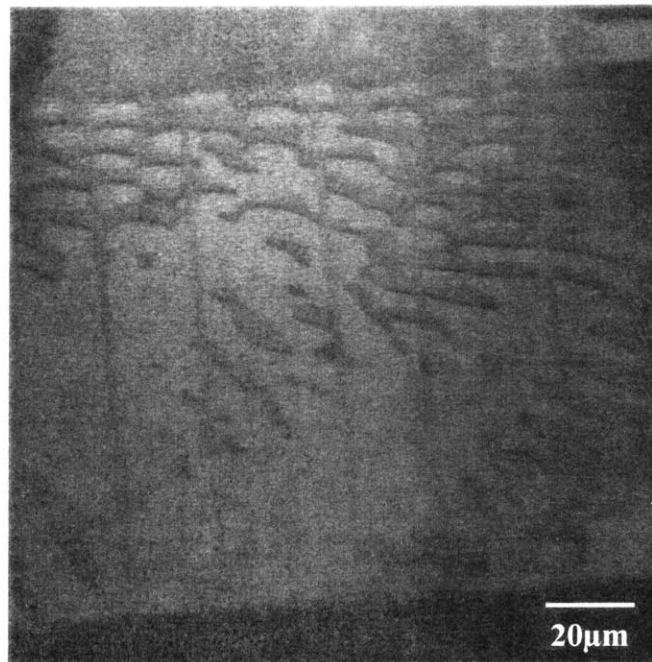
FIGURE 4.40   Sidewall trench due to poor contact during UV exposure
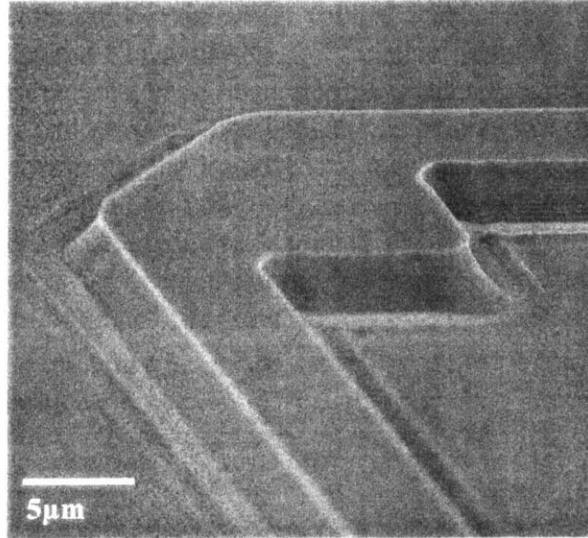
It was discovered that the exposure and development time greatly effected the side profile of the waveguide. Over exposure led to the rounding of waveguide side-walls, (Figure 4.41), while over-development will lead to undercutting, (Figure 4.42). An optimal exposure and development time was determined as 10 seconds and 1 minute and 30 seconds, respectively. The optimal time did not contain side-wall rounding and resulted in a greatly reduced undercut, Figure 4.43.

FIGURE 4.41   Over exposed sample. 30 second exposure and 1 minute development time

FIGURE 4.42   Over-developed sample.10 second exposure and 2 minute development time

FIGURE 4.43   Optimum exposure and development times of 10 seconds and 1 minute and 30 seconds, respectively

4.3 Reactive Ion Etching Results

Reactive ion etching (RIE) is a plasma-based etching technique where the material, which is etched, is removed as a volatile gaseous species [10]. Etching occurs by a chemical reaction between the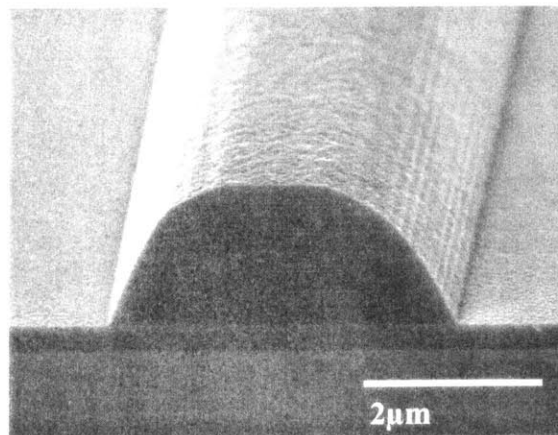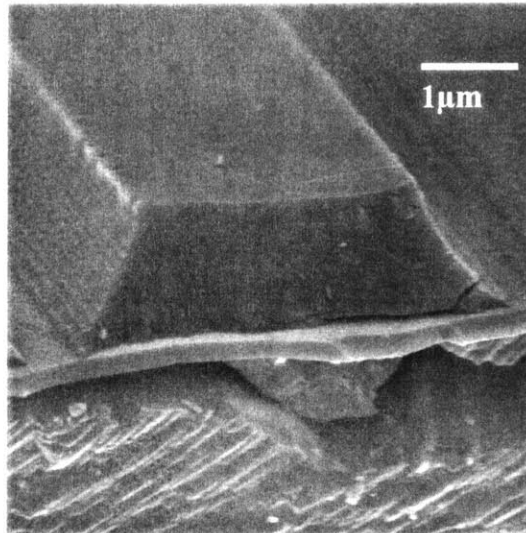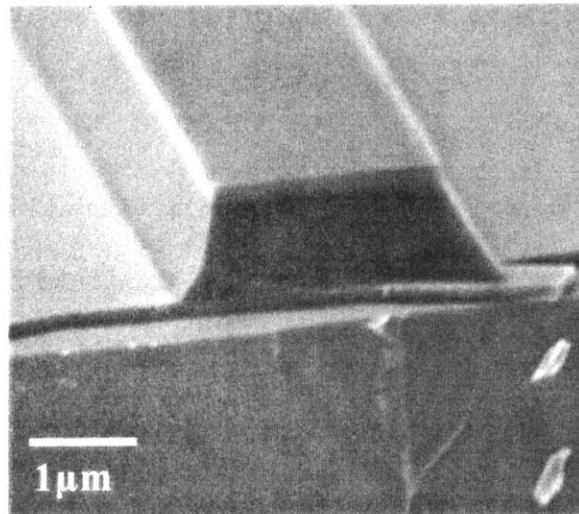 material to be etched and the atoms produced in the plasma. While choosing an etch mask, careful consideration on etching compatibility must be taken into account. With the use of an etch mask, reactive ion etching transfers the exposed pattern to the epilayers.

4.3.1 SiO_2 Reactive Ion Etch

The first step following the photolithography process is a CHF_3 plasma etch, using a PlasmaTherm RIE etcher, where the photoresist is used as the SiO_2 etch mask. CHF_3 will not etch through the resist mask, making it a suitable choice for the etch but there are difficulties with long etch runs. CHF_3 etches, when run for long periods of time, results in polymer deposition on the chamber walls. Therefore a CF_4 and O_2 clean run, as well as wiping the chamber with methanol, must be performed prior to and after each etch run. The CF_4 and O_2 clean run was performed for 15 minutes with the following parameters: 300W, 25mT and 350V. The CHF_3 plasma etch was performed for 15 minutes and 40 seconds three samples at a time. The parameters for the CHF_3 plasma etch were as follows: 300W, 10mT and 300V.

After successfully etching the SiO_2 layer using the photoresist as a mask, the pattern produced by photolithography has now been transferred to the SiO_2 layer. The next step in the process is to remove the top layer of photoresist with the use of an asher, a low powered O_2 RIE. To reduced the amount of time necessary for the ashing run, the sample is rinsed with acetone. Ashing was performed with a pressure of 3.5mT for 5 minutes. Figure 4.44 depicts a sample having undergone a RIE etch of SiO_2 and ash step. Notice on Figure 4.44 that there is still a small amount of residual photoresist left on top of the waveguide, this particular sample had not undergone a acetone rinse prior to ashing. The left over resist does not have an effect on later processing steps.

FIGURE 4.44   Results after RIE etch of SiO_2, using photoresist as a mask, and ashing. SiO_2 pattern above the epilayers is all that remains after the process

3μm
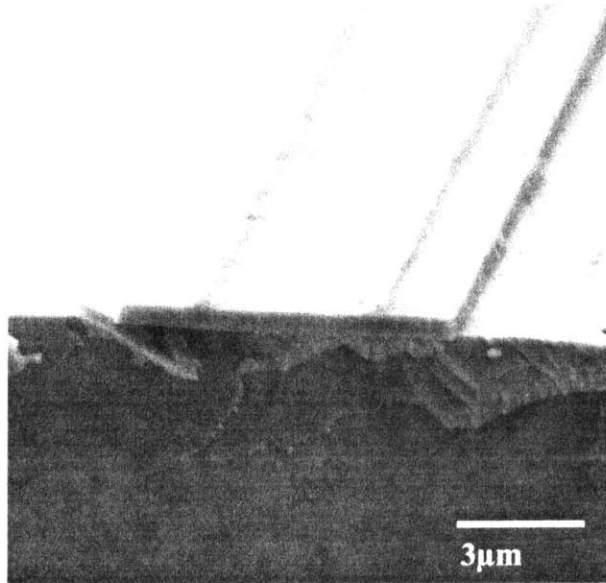
4.3.2 InP/InGaAsP Reactive Ion Etch

Once the waveguide patterns have been transferred to the SiO_2 layer, the sample is ready for a RIE etch of the InP/InGaAsP layers. Prior to etching the epilayers, a clean is first performed in the chamber. The clean was performed with O_2 and CF_4 with flow rates of 29.2 and 28.2 sccm, respectively. The InP/InGaAsP runs were performed with CH_4 and H_2 with flow rates of 10 and 20 sccm, respectively. The RF power that used for the run was approximately 100W and a DC bias of approximately 120V, produced an etch rate of 31nm/min. Due to a polymer by product of the CH_4 / H_2 etches, a cleaning run must be performed after every InP etching run. Since the final optical logic device will have a top layer of SiO_2, the SiO_2 hard mask is not removed.

4.3.3 InP/InGaAsP Reactive Ion Etching Problems & Solutions

Initial test runs were performed on blank InP samples. Desired results were achieved with CH_4 / H_2 flow rates of 10/20 sccm, pressure of 10mT and a RF power of 50W yielding an etch rate of 1μm/min, Figure 4.45. It was discovered that etching rates change when the same parameters were used with the InP/ InGaAsP structure. The first quaternary layer actual acted as an etch stop regard-

less of the etch duration, Figure 4.46. Decreasing the RF power to 150W and decreasing the pressure to 4mT, resulted in etching of both the quaternary layers as well as the InP. The use of 150W of RF also disintegrated the SiO_2 etch mask causing sputtered SiO_2 to be deposited on the substrate, Figure 4.46. A final optimization was made by reducing the RF power to 100W, Figure 4.48. Notice in Figure 4.48 the SiO_2 etch mask remains intact and there is an improvement in the sidewall smoothness. Also, upon careful expectation of Figure 4.48, the individual quaternary layers of the grown structures may been seen.

FIGURE 4.45   Initial RIE results performed on InP samples, RF power = 50W pressure = 10mT
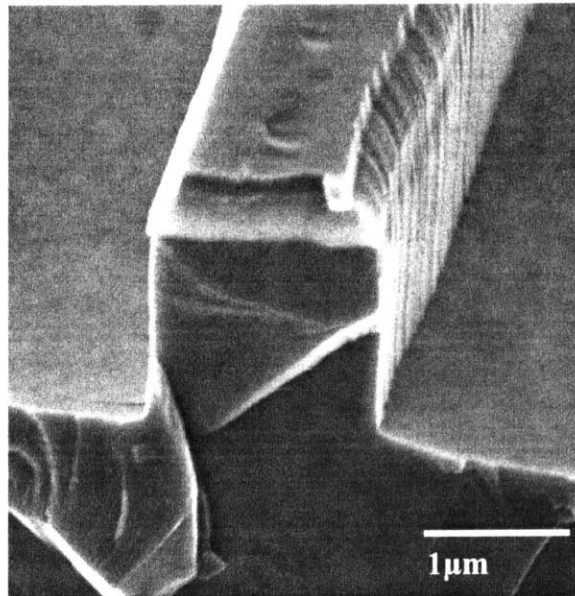
FIGURE 4.46   Initial RIE results performed on the InP/InGaAsP grown structure, RF power = 50W pressure = 10mT
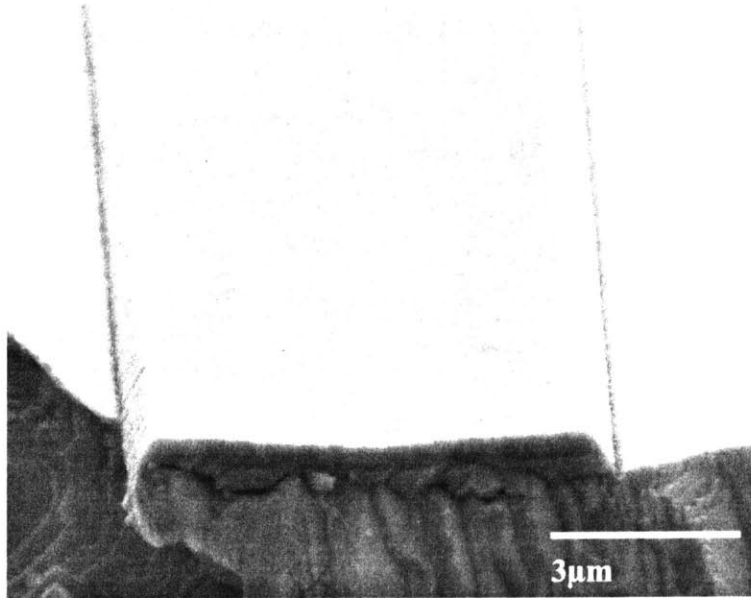

FIGURE 4.47   RIE results on the grown InP/InGaAsP substrate, RF power = 150W pressure = 4mT
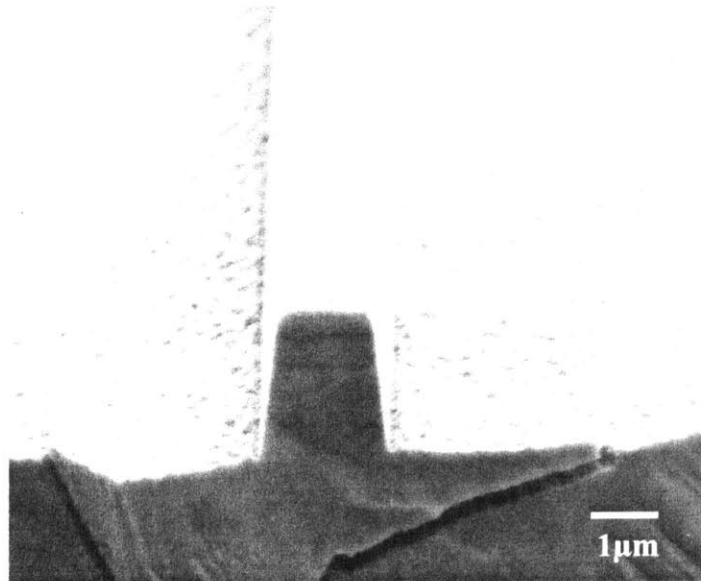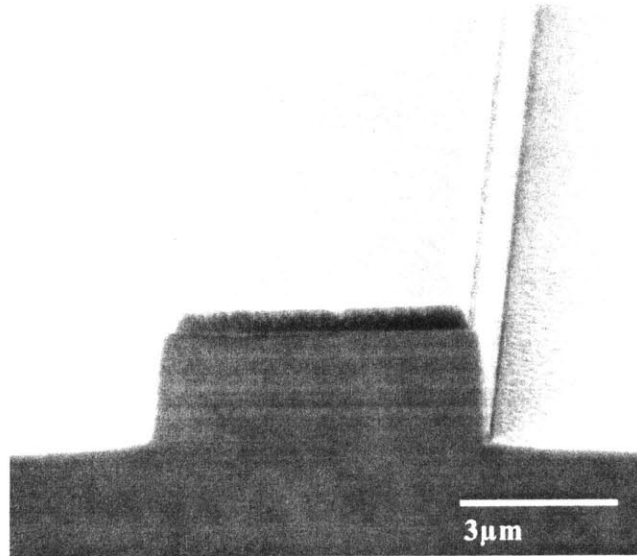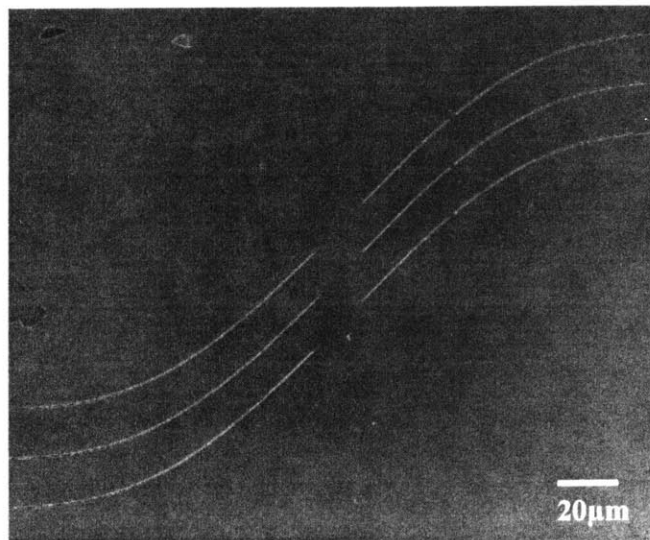
FIGURE 4.48   RIE results on the grown InP/InGaAsP substrate, RF power = 100W pressure = 4mT

3μm

Problems were also found with the Reactive Ion Etching of 1μm waveguides. Many of the 1μm waveguides contained breaks after the InP/InGaAsP RIE process, Figure 4.49.

FIGURE 4.49   1μm waveguide breaks due to the InP/InGaAsP RIE process

20μm

4.4 Images of Fabricated Waveguides

The following figures are SEM images of a few of the designed waveguide bends, which have gone through the entire fabrication process. Figure 4.50 and Figure 4.51 are examples of total internal reflections bends. Figure 4.52 depicts a set of offset bends, while Figure 4.53 shows a close-up view of one of the offsets. Figure 4.54 portrays a group of sine s-bends.

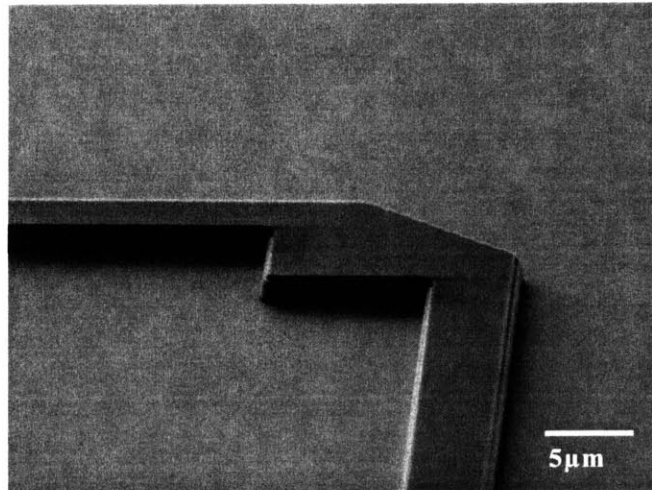**FIGURE 4.50**   Total Internal Reflection Bend, Resonator Bend

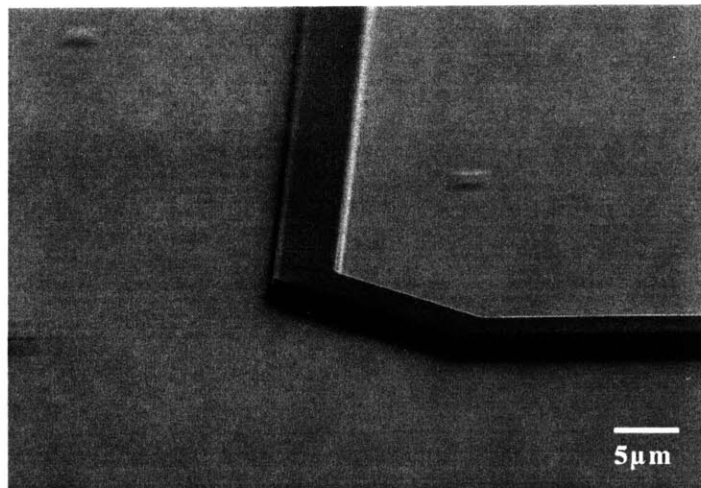**FIGURE 4.51**   Total Internal Reflection Bend, Corner Mirror Bend

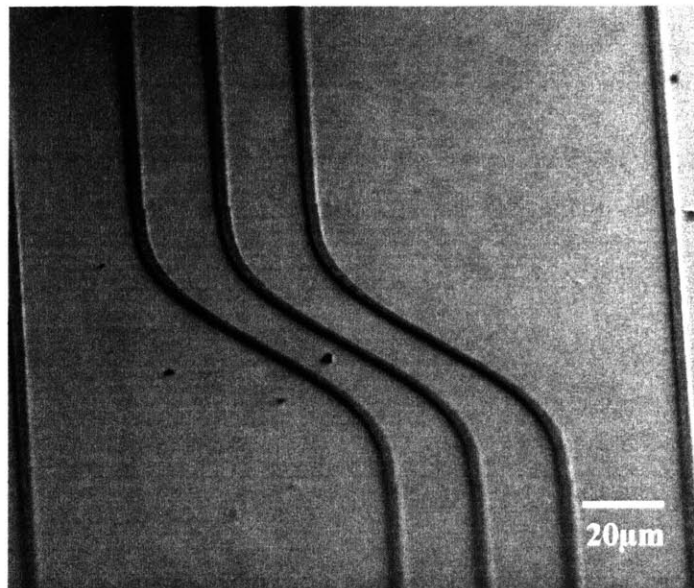**FIGURE 4.52**   A group of offset waveguide bends
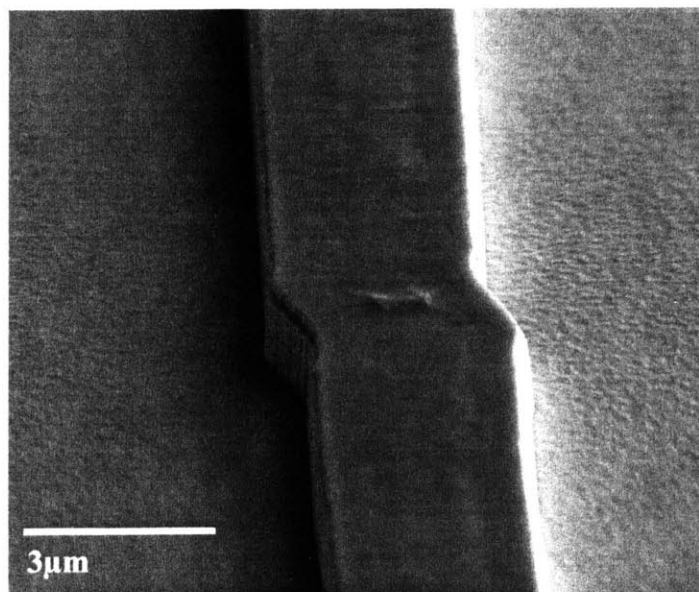

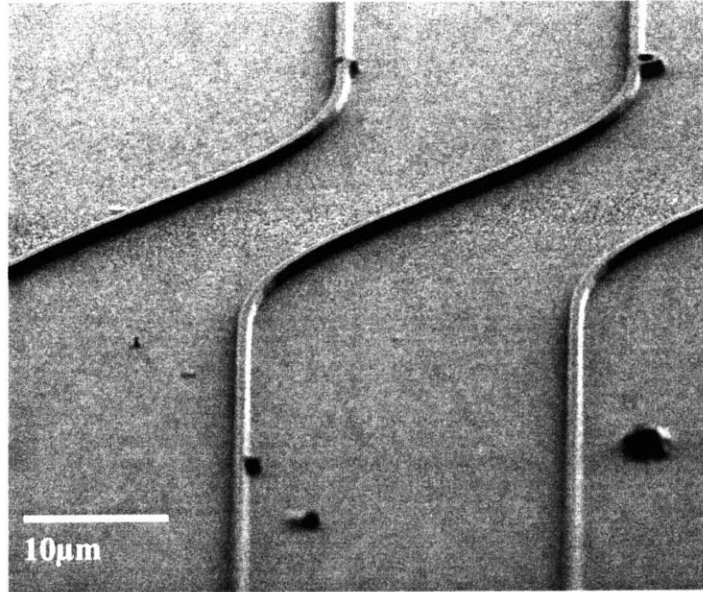**FIGURE 4.53**   Close up of an offset

**FIGURE 4.54**   A group of sine s-bends

5.0 MEASUREMENTS DISCUSSION & RESULTS

5.1 Measurement Procedure

5.1.1 Measurement Set-up

Measurements have been performed on a few of the fabricated waveguide samples. Figure 4.55 depicts a block diagram of the measurement set up used. The components in the set up were connected with the use of optical fibers, that was represented by the black arrows in the schematic. The computer contained a scanning Fabry-Perot program used to calculate the loss associated with each waveguide. The tunable laser was used to step through a variety of wavelengths used in the Fabry-Perot scanning method. The scanning program produced a wavelength vs. intensity plot. The polarization controller was used to obtain measurements for both TE and TM inputs. The sample was mounted on the piezo-electric controlled stage, which was used to position the waveguide in order to achieve maximum coupling.

FIGURE 4.55   Schematic of measurement set-up
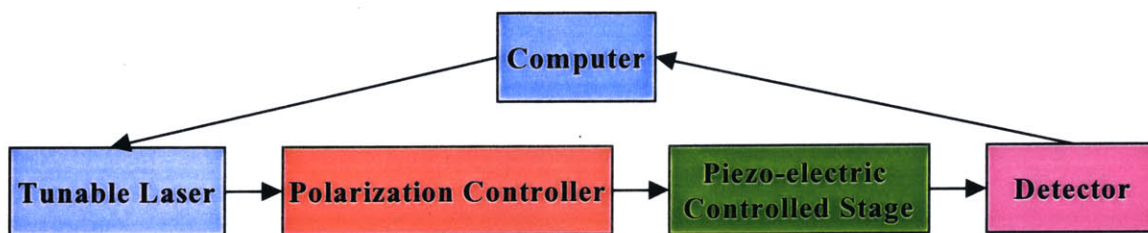
5.1.2 Measurement Set-up Limitations & Suggested Improvements

A typical Fabry-Perot scan will produce a sinusoidal graph of varying wavelength vs. intensity. A Fourier distribution of the produced graph will provide loss data on the measured device. Figure 4.56 portrays an example of a typical scanning Fabry-Perot result. Notice the second plot of Figure 4.56, the Fourier distribution results in a high peak symbolizing the fundamental mode. The smalls ripples to the right of the fundamental mode peak represent noise in the system, which should be significantly low in an ideal measurement set-up. Figure 4.57 contains an example of a Fabry-Perot scan obtained from one of the fabricated samples using the current measurement set-up. The Fourier distribution plot contained in Figure 4.57 contains very high noise levels.

FIGURE 4.56   An example of typical scanning Fabry-Perot results
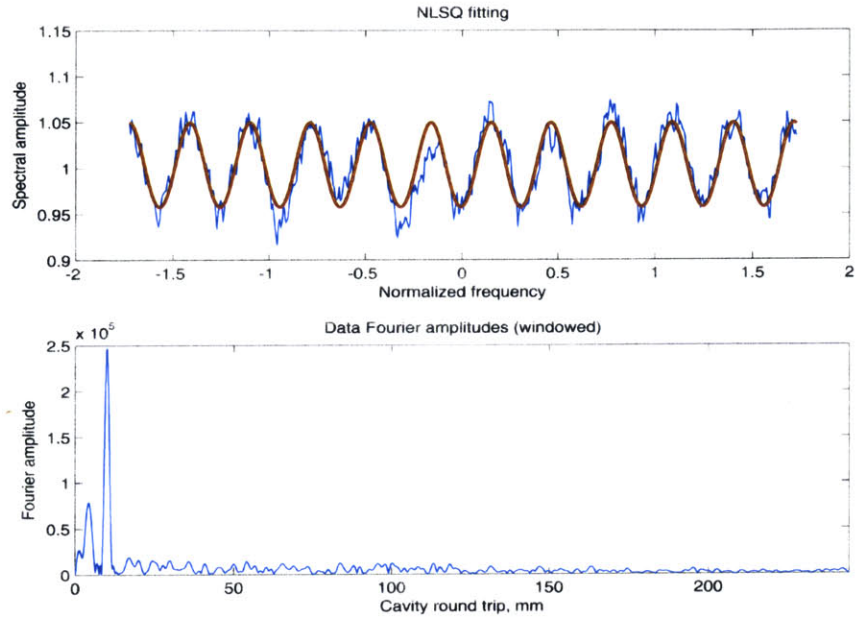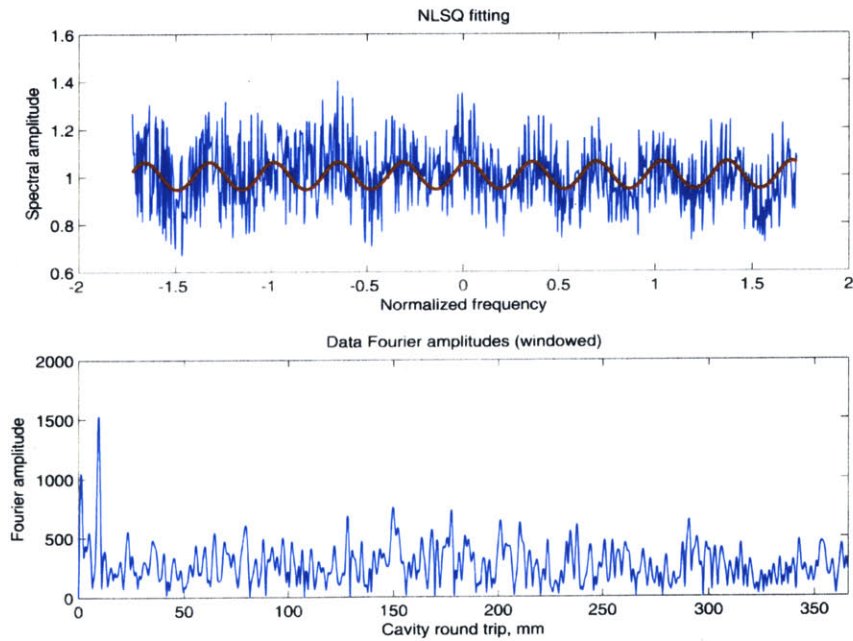

FIGURE 4.57   An example of scanning Fabry-Perot results using the current measurement set-up

The high amounts of noise in the system greatly elevated the amount of loss determined by the Fabry-Perot scan. Upon inspection of the initial loss measurements, the scanning Fabry-Perot technique was determined an unpractical method for finding loss in the current measurement set-up.

The failure of the Fabry-Perot scans prompted efforts towards obtaining a low noise measurement set-up. One of the major problems with the set-up was signal drift. After obtaining maximum coupling, the detected signal would decrease over time. A possible explanation for this is the use of a second optical fiber collecting the signal upon exiting the waveguide. The fiber, containing a diameter of approximately 125μm, may have possibly moved as a result of wind or table vibrations. A more appropriate substitution, for the fiber collecting the transmitted signal, would be a combination of an objective lens and detector. The objective lens would focus all the light transmitted through the waveguide and focus it in to the detector. The objective lens would therefore eliminate the problem of drift. Currently, maximum coupling is considered to be achieve once a maximum value has been recorded by the detector. A improved method would involve incorporating an infra-red camera and a monitor which would show the signal being transmitted through the waveguide. The infra-red camera would confirm the light is being transmitted through the center of the guide rather than 'blindly' guessing by using the detector readings. The use of a lock-in amplifier and chopper would also contribute to the effort of obtaining a more stable signal.

5.2 Measurement Results

Due to time constraints and limited resources, the following data was obtained using the original measurement set-up. The following plots were obtained by recording transmission measurements of the various waveguides. The data points represent averages of all the identical waveguides on the sample associated with the particular data point. A few samples contained data points which were not measurable do to bad cleaving, Figure 4.58. Cleaving a waveguide on a bent section created a curved and entry point, which is not ideal for fiber to waveguide coupling.

FIGURE 4.58   An example of a poorly cleaved waveguide
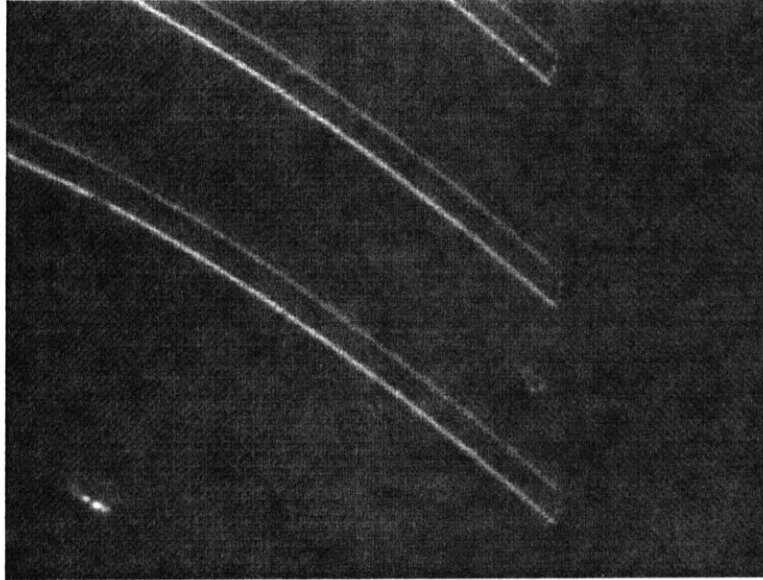
Four samples have been measured and compared Mask set A for layer A and B, widths 3μm and 4μm have been measured. The results for each sample is contained in two plots. The first is a plot containing the measurements of the four various bends and the straight waveguides. The second contains a plot of the four bends measured without the straight waveguides, to create a zoomed-in image of the results. All of the graphs are plotted with the parameters number of S-bends vs. (power detected/power incident).

Figure 4.59 portrays the measurement results of the layer A 4μm sample. As shown in the plot, all the waveguides show higher transmission occurs when the incident wave is TE, which is in agreement with the simulated results. Surprisingly, the smallest radius, 109.32μm, is not the most lossy waveguide. For waveguides containing only two bends, a radius of 109.32μm transmits a significant amount more than that of a waveguide with a radius of 142.53μm also containing two bends. Both waveguides containing bends of radii 109.32μm and 142.53μm yield similar results when the number of bends is more than two. As expected, the waveguide containing the largest radius, 365.59μm, contains the least loss of the bent waveguides.

Figure 4.60 displays the measurement results of the layer B 4μm sample. The measurements show TM incident waves transmitting more light compared to the TE waves. According to the simulated results of the modal profiles, the opposite is

expected. The simulations show TE modes having a higher modal index than TM modes. Therefore TE modes contain better modal confinement and in theory should produce less loss. Once the polarization has been set by the polarization controller, movements in the input optical fiber may shift the polarization state of the light coming into the waveguides. A possible explanation for the measurement results showing TM modes having greater transmission, may be the result of shifting the polarization of the fiber while adjusting for maximum coupling. Another unexpected result is the transmission of the waveguides increasing with an increase of four bends to six. This result is best explained by the signal drift caused by the moving fibers or the measurements being taken while the fibers are not maximally coupled. Again, the largest waveguide bend, radius of 365.59μm, is the bend which contains the least loss, as was expected. layer B seems to transmit less of the signal as compared to layer A waveguides of the same width.

Figure 4.61 contains the results of a sample with layer A, bend set A and a waveguide width of 3μm. Figure 4.62 contains the results of a sample with layer B, bend set A and a waveguide width of 3μm. Upon inspection of these two figures, radii 109.32μm and 142.53μm give similar results for both layer A and B. Radii 365.59μm and 179.85μm for layer A and layer B give different results. Layer A shows greater amounts of loss for the two larger radii when compared to layer B. The opposite may been seen when comparing the two layers with waveguide thickness of 4μm. Layer A does not consistently show TE or TM modes having more loss. Layer B shows TM providing better transmission.

When analyzed and compared, the measurements provide results which are unexpected and inconsistent. The measurement set-up currently being used is unrelaiable. Future measurements should be preformed on a more suitable set-up.

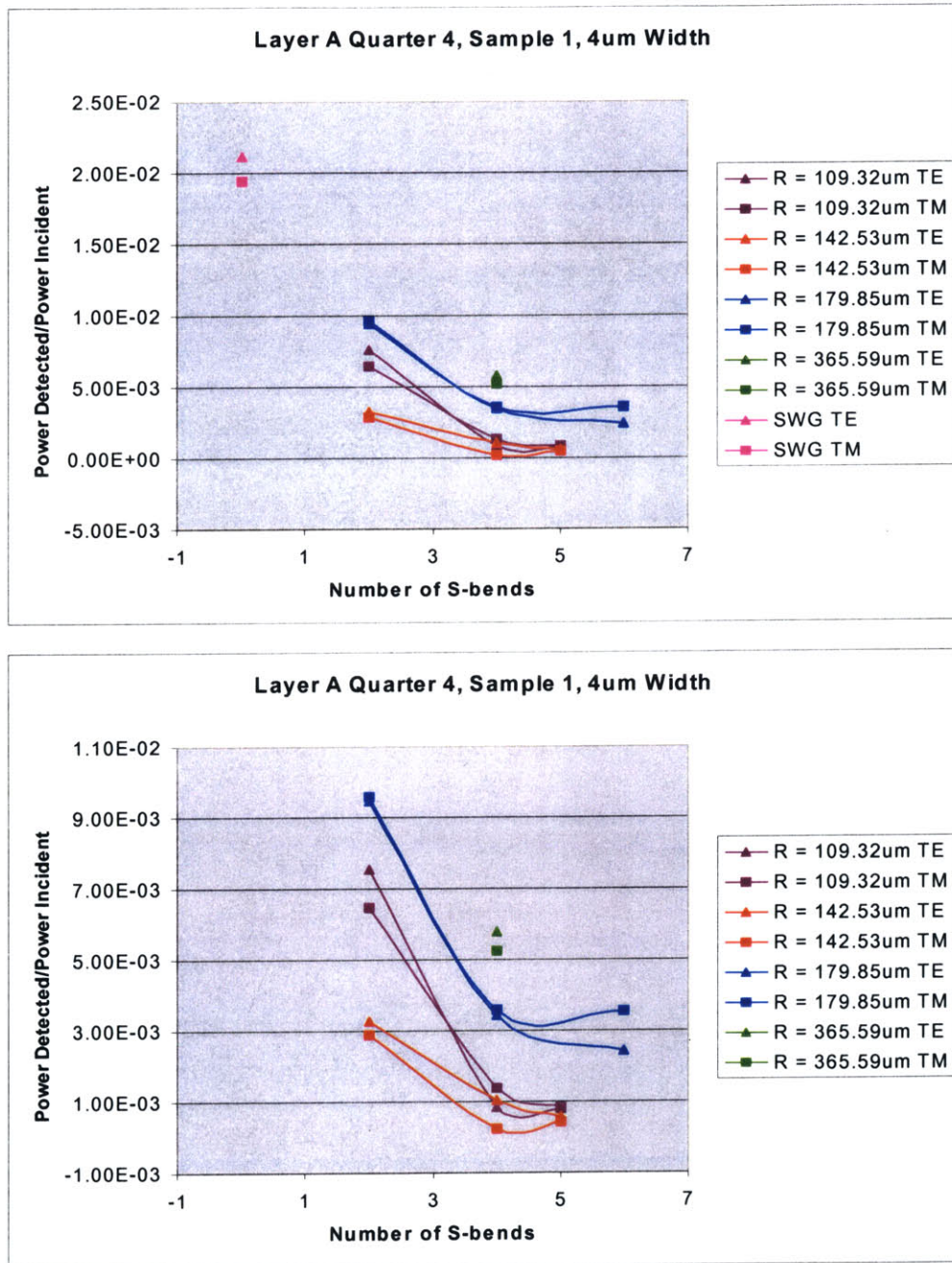**FIGURE 4.59** Measurement results of Layer A. Waveguide width is 4μm. Bend set A

FIGURE 4.60   Measurement results of Layer B. Waveguide width is 4μm. Bend set A

FIGURE 4.61   Measurement results of Layer A. Waveguide width is 3μm. Bend set A

FIGURE 4.62   Measurement results of Layer B. Waveguide width is 3μm. Bend set A
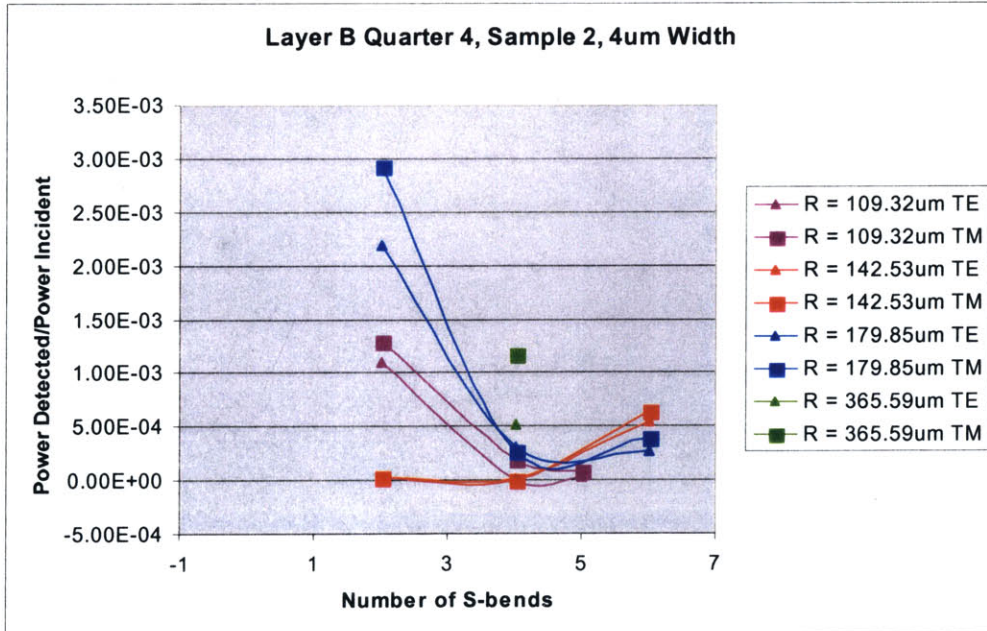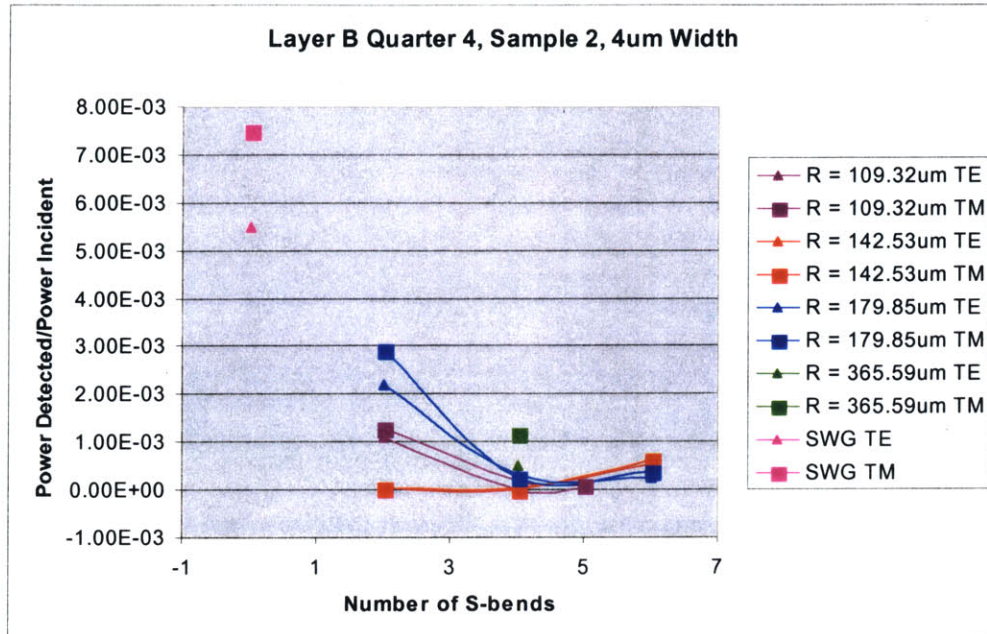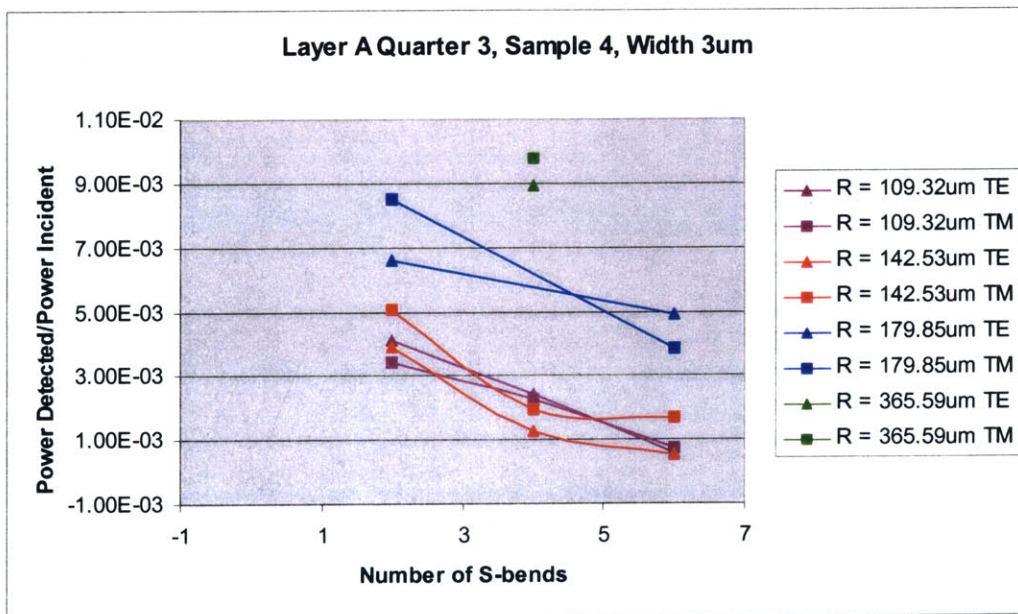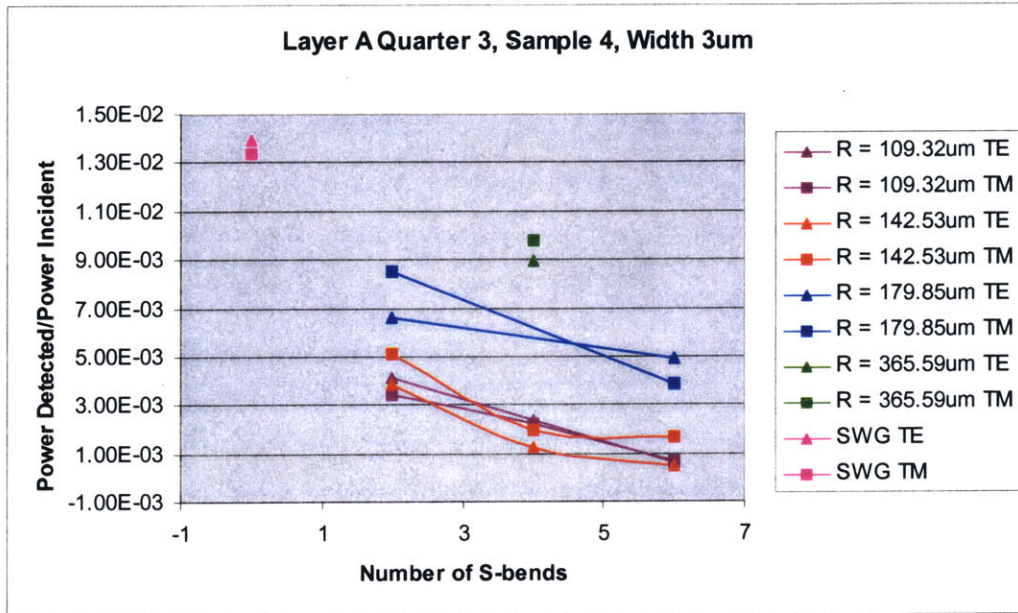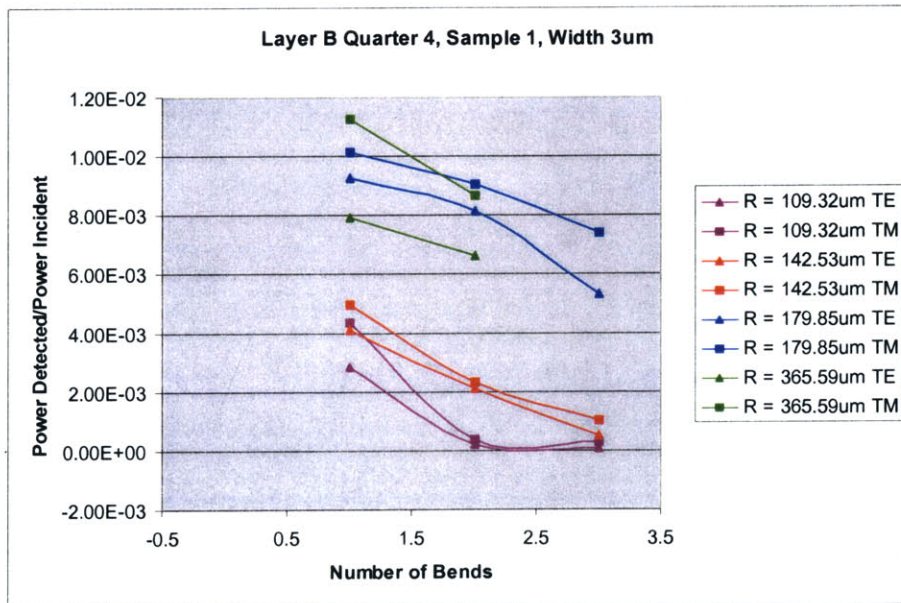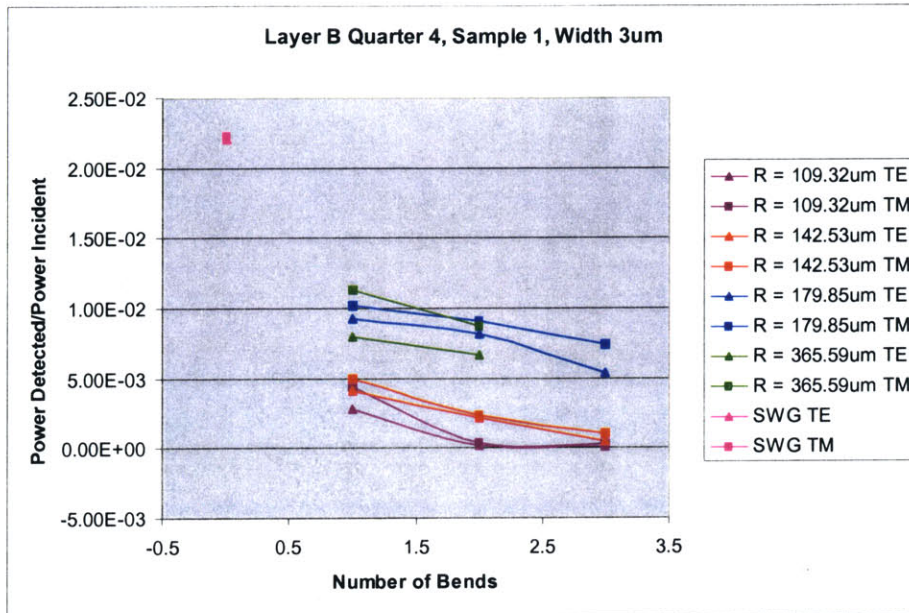
6.0 CONCLUSION

Finding a solution for low loss compact waveguide bends is essential for reducing the size of future photonic integrated circuit devices. In this Master's thesis, a solution for low loss compact waveguide bends has been investigated. A survey of past work was conducted, where ideas on bend geometry and waveguide dimensions were derived from. Simulations on straight waveguide sections were performed in order to analyze the waveguide mode of various widths. Fabrication steps have been outlined and results stated. Measurements have been performed to determine the mode and bending loss of the various waveguides.

Simulated results show a 4μm width waveguide produces the best modal confinement for the layer A growth. The simulated results obtained for the layer B growth seem unlikely and should be compared to future measured results. A fabrication process flow has been developed which provides good reproducible results. However, fabrication problems did occur with 1μm and 2μm waveguide widths. Measurements have been performed. The current measurement set-up was not capable of producing reliable results. High noise levels were believed to be the reason behind the inconsistent results. An improved method for taking measurements has been suggested.

7.0 REFERENCES

[1] G. P. Agrawal, <u>Fiber-Optic Communication Systems</u>, *John Wiley & Sons, Inc,* 1997, pp. 24-26

[2] D. H. Staelin, A. W. Morgenthaler, J. A. Kong, <u>Electromagnetic Waves</u>, *Prentice Hall,* 1998 pp. 141-146.

[3] http://floti.bell.ac.uk/MathsPhysics/1total.htm

[4] M. Koshiba, <u>Optical Waveguide Analysis</u>. McGraw - Hill, Inc. 1990 pp

[5] Michael W. Austin. "GaAs/GaAlAs Curved Rib Waveguides." IEEE Transactions on Microwave Theory and Techniques, Vol. MTT-30, No. 4, pp. 641-646, April 1982.

[6] M. Rajarajan, S.S.A Obayya, B.M.A Rahman, K.T.V. Grattan and H.A.El-Mikati. "Characterisation of low-loss wavguide bends with offset-optimisation of compact photonic integrated ciruits." IEEE Proc.-Optoelectron., Vol. 147, No. 6, pp. 382-388, December 2000.

[7] Chulhun Seo, Jerry C. Chen. "Low Transition Losses in Bent Rib Waveguides." IEEE Journal of Lightwave Technology, Vol. 14, No. 10, pp. 2255-2259, October 1996.

[8] Christina Manolatou, "Passive Components for Dense Optical Integration Based on High Index Contrast", PhD. Thesis, MIT (2001)

[9] M. Dagenais, R. Leheny, J. Crow, <u>Integrated Optoelectronics</u>, *Academic Press Inc.,* 1995 pp. 83-100.

[10] H Smith, <u>Submicron and Nanometer Stuctures Technology</u>, *NanoStructures Press,* 1994 ch 24.